Synthetic Aperture Radar (SAR) for Ocean: A Review

Reza Mohammadi Asiyabi, *Member, IEEE*, Arsalan Ghorbanian, Shaahin Nazarpour Tameh, Meisam Amani, *Senior Member, IEEE*, Shuanggen Jin, *Senior Member, IEEE*, and Ali Mohammadzadeh

***Abstract*—Oceans cover approximately 71% of the Earth's surface and provide numerous services to the environment and humans. Precise, real-time, and large-scale monitoring of the oceanographic parameters is essential for ocean conservation and understanding the interactions between oceans and the atmosphere. In this regard, synthetic aperture radar (SAR) systems, with unique capabilities (e.g., day-night and almost all-weather data acquisition), provide valuable datasets for ocean studies. Many studies have exploited the applications of SAR imagery for oceans and have proposed numerous methods to study oceanographic parameters. In this study, a brief introduction to SAR and the interaction between microwave signals and the ocean surface are initially provided. Then, the important spaceborne and airborne SAR systems for oceanographic applications are summarized. Subsequently, 12 different applications of SAR systems in the ocean are comprehensively discussed, and the advantages and disadvantages of SAR systems for ocean studies are extensively explored. Finally, the research trend on SAR applications in the ocean is provided by analyzing all the relevant papers published between 1973 and the end of December 2022, and the existing challenges are discussed for future studies.**

***Index Terms*—Ocean currents, ocean wave, ocean wind, oil spill, remote sensing, sea ice, sea level, ship detection, synthetic aperture radar (SAR).**

I. Introduction

ACTIVE microwave remote sensing (RS) systems were first utilized before World War II (the 1930s and 1940s) for military applications. However, the first efforts to understand the electromagnetic (EM) scattering of the ocean waves go back to the 1960s and 1970s when the U.S. Naval Research Laboratory performed pioneering laboratory and field measurements, which were later followed by the field measurements of the National Aeronautics and Space Administration (NASA) [1]. For example, during the 1960s, Moore and Pierson [2] suggested that ocean waves and wind speed could be derived from radar data. According to this idea and the theoretical developments in the field of radar technology, several ground surveys and airborne missions were initiated, which led to the first microwave sensor on the Skylab mission for ocean observation by NASA in 1973–1974 [3]. Despite its short operation, the Skylab mission facilitated NASA's first oceanographic satellite, SeaSat-1, launched in 1978 [4], [5]. SeaSat-1 demonstrated the advantages of spaceborne active microwave sensors for oceanographic applications and motivated many successful Earth Observation (EO) missions in the 1990s, including European Remote Sensing Satellites (ERS-1 and 2), RADARSAT-1, and Advanced Earth Observing Satellite, respectively launched by the European Space Agency (ESA), Canadian Space Agency (CSA), and National Space Development Agency (NASDA) of Japan [1], [6].

Since the launch of SeaSat-1, synthetic aperture radar (SAR) has played an important role in many different applications, including oceanography. Currently, many spaceborne microwave RS systems are in orbit and are being operationally used for ocean studies. Moreover, various airborne microwave systems have also been developed for local-scale ocean applications. For example, SAR systems have been effectively employed for ocean wave imaging [7], bathymetric mapping [8], ocean current studies [9], wind speed/direction estimation [10], oil spill detection [11], ship detection [12], and ice shelf monitoring [13]. Furthermore, several programs and services have been set up for oceanographic applications of the EO data, especially using SAR images. For instance, the Copernicus Marine Service (or Copernicus Marine Environment Monitoring Service—CMEMS) is the marine environment monitoring service as a part of the Copernicus Programme of the European Union [14]. CMEMS uses a vast amount of ground-based, airborne, and spaceborne (including spaceborne SAR images) to provide free, frequent, and systematic authoritative information on the state of the Blue (physical), White (sea ice) and Green (biogeochemical) ocean, on a global and regional scales [14].

Many studies have discussed the applicability of SAR systems for specific oceanographic applications [15], [16], [17], [18], [19], [20], [21], [22]. In addition, several studies provided

Manuscript received 24 May 2023; revised 17 July 2023; accepted 20 August 2023. Date of publication 30 August 2023; date of current version 13 October 2023. *(Corresponding author: Meisam Amani.)*

Reza Mohammadi Asiyabi is with the Center for Spatial Information (CEOSpaceTech), University Politehnica of Bucharest, 060042 Bucuresti, Romania (e-mail: reza.mohammadi@upb.ro).

Arsalan Ghorbanian and Ali Mohammadzadeh are with the Department of Photogrammetry and Remote Sensing, Faculty of Geodesy and Geomatics Engineering, K. N. Toosi University of Technology, Tehran 19967-15433, Iran (e-mail: a.ghorbanian@email.kntu.ac.ir; a_mohammadzadeh@kntu.ac.ir).

Shaahin Nazarpour Tameh is with the Department of Civil, Chemical and Environmental Engineering (DICCA), University of Genoa, 16145 Genoa, Italy (e-mail: shaahin.nazarpour.tameh@edu.unige.it).

Meisam Amani is with the School of Surveying and Land Information Engineering, Henan Polytechnic University, Jiaozuo 454000, China, and also with the WSP Environment and Infrastructure Canada Limited, Ottawa, ON K2E 7L5, Canada (e-mail: meisam.amani@woodplc.com).

Shuanggen Jin is with the School of Surveying and Land Information Engineering, Henan Polytechnic University, Jiaozuo 454000, China, and also with the Shanghai Astronomical Observatory, Chinese Academy of Sciences, Shanghai 200030, China (e-mail: sgjin@shao.ac.cn).

Digital Object Identifier 10.1109/JSTARS.2023.3310363

reviews on different RS systems, including SAR imagery for oceanography [23], [24], [25], [26], [27], [28], [29]. Several advancements in SAR imaging instruments, as well as data processing techniques for oceanography, have been achieved in the last few years. However, to the best of the author's knowledge, there is not a recent comprehensive review on SAR systems for oceanographic studies. This study provides a comprehensive review of the oceanographic applications of various spaceborne and airborne SAR systems. A brief introduction of the interaction between the transmitted microwave signal and the ocean surface is first provided, and different available SAR systems are discussed. The main part of this review paper discusses 12 oceanographic applications of the SAR systems along with their advantages and disadvantages. Then, a general outline of the publication trends in this field is provided. The main objectives of this study can be summarized as follows.

1) A simple and brief introduction on the interaction of the transmitted radar signal and the backscattering surface is provided, which will be beneficial for the new researchers in the SAR field to better understand the mechanism of the SAR imaging systems.
2) SAR spaceborne and airborne systems are extensively reviewed, and their different attributes are summarized.
3) A comprehensive review of different oceanographic applications of SAR imagery systems is provided with several case studies.
4) The main advantages and disadvantages of SAR images for oceanographic applications are discussed.
5) A thorough review of the publication trends in the field of oceanographic SAR applications is conducted from 1973 until the end of December 2022.

II. Principles of SAR Systems for Ocean

Generally, active microwave systems are divided into two distinct categories: imaging and nonimaging systems [30]. Nonimaging microwave systems (e.g., altimeters and scatterometers) measure in one dimension and cannot provide two-dimensional (2-D) images. These systems measure the time delay of the transmitted signal (i.e., altimeters) or the amount of the backscattered energy (i.e., scatterometers) in one linear dimension [30]. On the other hand, imaging microwave systems measure the time delay and the amount of the backscattered energy from the transmitted signal in two dimensions and, thus, provide 2-D images. SAR is the most common form of active microwave imaging system [30].

SAR imaging systems have become one of the primary high-resolution EO sensors used for ocean studies due to their unique capabilities. For example, SAR measurements are sensitive to small roughness changes in the ocean surface and are independent of solar illumination and weather conditions. They also have controllable properties, including power, frequency, phase, polarization, incident angle, spatial resolution, and swath width [31].

Despite enormous benefits, SAR imagery is relatively complex. The ocean's motion further complicates the SAR data interpretation. SAR imaging systems transmit EM waves with microwave frequencies and receive the backscattered signals from the target surface. Most of the SAR systems operate in wavelengths between 3 to 75 cm (i.e., equivalent to X, C, S, L, and P bands). This enables the SAR signals to pass through the clouds (almost unchanged) and provide high-quality data, even over cloudy regions [1], [31]. The returned signal from the ocean to the SAR sensor is a complex interaction of the transmitted signal and the backscattering energy from the ocean surface. A variety of factors, including the characteristics of the transmitted signal (e.g., frequency, polarization, and imaging geometry) and those of the ocean (e.g., roughness, waves' interaction in different scales, oceanic currents, and presence of oil slicks or ships on the water surface) affect the SAR signal return [32], [33]. For instance, when the ocean surface is perfectly flat (without wave), it behaves like a specular reflector, which reflects a considerable amount of the transmitted signal in the opposite direction and, consequently, appears dark in monostatic radar imagery [31], [33]. The SAR signal is very sensitive to the interactions between the ocean surface and wind. Generally, when wind speed is between 2 and 14 m/s, it sufficiently roughens the ocean surface to be measured by SAR systems [6], [34].

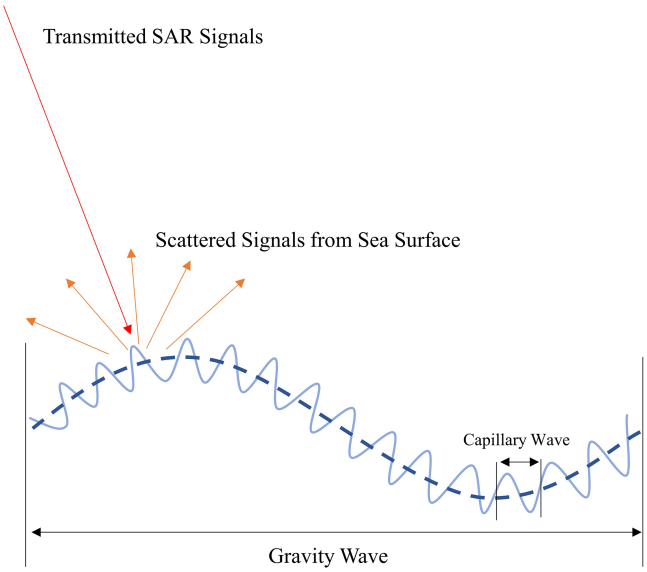

Fig. 1. Gravity and capillary waves on the ocean surface.

There are generally two types of waves on the surface of the oceans: gravity and capillary waves. As illustrated in Fig. 1, gravity waves result from gravitation acting on the disturbed mass of water to counteract the effect of the wind, while capillary waves are the water surface tensions to act against the wind disturbances [33], [35]. Gravity waves tend to have a longer wavelength than capillary waves, but their heights depend on the wind speed, fetch length, and wind duration [33].

As a result of the periodicity of the ocean waves and their highly dynamic nature, there may be a large range of wavelengths associated with the waves. The periodicity and different wavelengths of the ocean waves make the Bragg scattering mechanism suitable for describing the nature of the ocean surface from the SAR imagery [31], [33], [36]. The radar

backscattering can be described by the Bragg scattering mechanism when the wavelength of the transmitted signal and wavelength of the ocean wave have the relationship as follows [31], [32]:

$$\lambda_B = \frac{\lambda_R}{2\sin\theta} \tag{1}$$

where λ_R and λ_B are radar signal and ocean wave wavelengths, respectively, and θ is the radar incident angle. Although the backscattered signal is primarily influenced by Bragg scattering, non-Bragg scattering mechanisms, such as surface and breaking waves, also have a significant impact on the backscattered signal and should be taken into consideration [37]. Several mathematical descriptions of the radar signal scattering process are provided in the literature [21], [31], [38], [39], [40]. A short and simple description is provided in this section based on the formulations provided in [31], [39], [40].

The transmitted radar signal can be represented by the following:

$$E_t(x) = E_0 e^{-kx\,\sin\theta_t} \tag{2}$$

where $k = 2\pi/\lambda$ is the wavelength parameter of the transmitted radar signal. The subscript "*t*" in the incident angel (θ_t) represents the transmitted signal; x is the propagation distance of the signal; and E_0 is the magnitude of the incident wave. Similarly, the reflected radar energy, $E_r(x)$, can be derived by multiplying the reflection co-efficient, Γ, with the $E_t(x)$ as shown in the following:

$$E_r(x) = \Gamma E_0 e^{-kx\,\sin\theta_t}. \tag{3}$$

The reflection coefficient, Γ, is also used to represent the scattered signal, $E_s(x)$, as shown in the following:

$$E_s(x) = \xi(\theta_t,\ \theta_a,\ D)\,\Gamma E_0 \tag{4}$$

in which ξ represents the antenna radiation pattern, and is a function of the incidence angle, θ_t, antenna radiation angle, θ_a, and differential surface length, D [31], [39], [40]. As a result, the radar cross section for the ocean surface is proportional to the reflection coefficient, Γ, and the antenna radiation pattern, ξ, as shown in the following:

$$\sigma \propto \Gamma^2 \sum_{k=1}^{n} \{\xi\langle(\theta_t + \alpha_k), -(\theta_a + \alpha_k),\ D_k\rangle\}^2. \tag{5}$$

The slope angle of the kth differential surface length in (5) is represented by α_k. The dependence of the radar backscattering cross section, σ, on the polarization and frequency of the transmitted signal can be explained by the Length parameter, ϖ_{rt}, where "*r*" and "*t*" represent the polarization of the received and the transmitted signals, respectively. Therefore, the radar backscattering cross-section for each polarization can be represented by the following:

$$\sigma_{rt} = 8k^4h^2\cos^4\theta_i|\varpi_{rt}|^2\,F(2k\,\sin\theta_i) \tag{6}$$

where *F(k)* is the Fourier transform of the surface correlation function, and h is the surface perturbation. The surface perturbation can be used for the Rayleigh Criterion to define the relative roughness of the surface. In order to better describe the interaction between the radar signal and the backscattering surface, the length parameter, ϖ_{rt}, is useful. As mentioned before, radar frequency and incidence angels affect the length parameter. However, the effect of the radar signal frequency on the length parameter is obscure. This is because the radar frequency directly affects the complex dielectric constant or permittivity, ϵ, of the backscattering surface, which influences the radar backscattered signal. Consequently, the Length parameter for the HH and VV polarizations can be defined using the incidence angle, θ_i, and permittivity, ϵ, as shown in the following:

$$\varpi_{HH} = \frac{\cos\theta_i - \sqrt{\epsilon - \sin^2\theta_i}}{\left(\cos\theta_i + \sqrt{\epsilon - \sin^2\theta_i}\right)^2} \tag{7}$$

$$\varpi_{VV} = (\epsilon - 1)\,\frac{\sin^2\theta_i - \epsilon\left(1 + \sin^2\theta_i\right)}{\left(\epsilon\cos\theta_i + \sqrt{\epsilon - \sin^2\theta_i}\right)^2}. \tag{8}$$

Furthermore, incidence angle is one of the most important parameters of the SAR instruments for ocean applications. At smaller incidence angles, higher sea surface returns are usually observable, and the returned energy rapidly decreases as the incidence angle increases. Therefore, most of the oceanographic SAR satellite missions employ incidence angles of around 20° to take advantage of those higher available energies [33]. Moreover, the sea surface appears dark in higher incidence angles (around 40°) which makes other objects on the sea surface (e.g., ships or oil rigs) more apparent. The dependency of the radar backscatter on the incidence angle enables observing gravity waves on the sea surface due to Bragg's resonance with the capillary waves. The front slope of the gravity waves results in a smaller incidence angle because they face the transmitted radar signal and, thus, appear brighter in SAR images due to the increased returned energy. On the other hand, the back slopes increase the incidence angle and appear relatively darker [33].

Generally, anything that affects the capillary waves of the sea surface (e.g., wind speed/direction and dampening by rain or other mechanisms, such as oil slicks) modulates the radar backscatter [32]. Internal ocean waves, which are generated by mechanisms that cause underwater disturbances (e.g., river inflows, movement of water over varying bottom topography, and underwater earthquakes), also affect the capillary waves of the sea surface and, therefore, can be observed using SAR images [33].

III. SAR Systems for Ocean Applications

A. Spaceborne SAR Systems

As mentioned in the introduction section, after successful testing of the spaceborne SAR systems during the Skylab mission in 1973–1974, SeaSat-1 was the first SAR satellite launched on June 27, 1978 and continued its mission until October 1978 [41], [42]. The SAR sensor of SeaSat-1 was operating at the L-band frequency and the HH polarization with a fixed 100 km swath width and 20° to 26° incident angles [42]. After the successful experiment of SeaSat-1, NASA launched the Shuttle Imaging RADAR-A (SIR-A) in 1981, which was a single channel L-band

HH SAR system. SIR-B, a single digital channel L-band HH SAR system with variable incident angles, was launched in 1984 [6], [32].

ESA launched ERS-1 in 1991, which collected data in C-band and VV polarization with 100 km swath width and 20° to 26° incident angles. ERS-2 with the same properties along with multiple enhancements was also launched in 1995 [32], [42]. JERS-1, launched by the Japanese Space Agency, collected radar data in L-band and HH polarization with 32° to 38° incident angles between 1992 and 1998 [32]. Furthermore, a collaboration between NASA, the German Space Agency, and Italian Space Agency in 1994 led to a revolutionary Shuttle Imaging RADAR-C/X-band SAR (SIR-C/XSAR), which was the first three frequency (L/C/X-bands) and fully polarimetric (HH/VV/HV/VH for L/C-band, and HH for X-band) spaceborne SAR instrument [42]. Another successful SAR mission in the 1990s was RADARSAT-1 by the CSA, which was launched in 1995. RADARSAT-1 was a C-band HH SAR system with variable incident angles and swath widths [43].

Following these missions, many spaceborne SAR instruments have been launched with different imaging properties and have so far provided valuable data for oceanography in addition to other applications. The increasing number of SAR satellites in the past two decades has provided unprecedented opportunities for various oceanographic applications. For instance, RADARSAT-2 was launched in December 2007 by the CSA and MacDonald Dettwiler Associates Ltd. to continue the legacy of RADARSAT-1 and has been utilized for many oceanographic applications since then [43]. RADARSAT-2 is a state-of-the-art technology that provides fully polarimetric SAR data in C-band with 3–100 m spatial resolution [43].

The advanced synthetic aperture radar (ASAR) sensor onboard the Envisat was developed by ESA based on the AMI-SAR flown on ERS-1 and ERS-2 [44]. ASAR was a C-band imaging radar instrument with various imaging modes and five polarization modes (VV, HH, VV+HH, HV+HH, or VH+VV). Envisat was launched in March 2002 and provided valuable data for oceanography and many other applications until April 2012 [45].

Another well-known SAR mission for oceanographic applications is Sentinel-1, the first satellite of the Copernicus mission, which has been designed and launched by ESA. Sentinel-1 is composed of a constellation of two satellites, Sentinel-1A and Sentinel-1B, that were launched in April 2014 and April 2016, respectively. They share the same orbital plane with a 180° orbital phasing difference. This constellation enhances the revisit time and coverage of the mission. In addition, Sentinel-1C and D are planned to be launched in 2022 and 2023, respectively. Sentinel-1 acquires data in C-band and Dual polarization (VV+VH or HH+HV). Sentinel-1 data is freely available through the Copernicus-hub (https://scihub.copernicus.eu/) [46].

TerraSAR-X is a German SAR satellite mission managed by the German Aerospace Center (i.e., DLR). It was launched in June 2007, and since then, it has been providing high-resolution X-band data for a wide range of applications, including oceanography. TerraSAR-X is capable of acquiring data in single, dual, and quad polarization modes [47]. TanDEM-X is also a DLR SAR mission which is a high-resolution interferometric add-on to the TerraSAR-X for digital elevation measurements and was launched in June 2010 [47].

Advanced land observation satellite (ALOS) is a Japanese SAR system developed by the Japan Aerospace Exploration Agency (JAXA; formerly NASDA) and was launched in January 2006. Phased-array L-band synthetic aperture radar (PALSAR) sensor onboard ALOS provided valuable high-resolution L-band SAR data from the ocean with multi-polarization and various imaging modes. ALOS ended in April 2011, with ALOS-2, carrying the PALSAR-2 sensor with multiple enhancements from PALSAR, was launched in May 2014 [42], [48].

The China National Space Administration (CNSA) also launched its first civilian C-band polarimetric SAR mission, Gaofen-3, in August 2016. Gaofen-3 is capable of 12 different SAR data acquisition modes with single, dual, and quad polarization and up to 1 m resolution [49].

The RADARSAT Constellation Mission (RCM) consists of three identical EO satellites and was launched on June 12, 2019 by the Canadian Space Agency. The primary goal of RCM is to provide C-band data continuity for RADARSAT-2 users. RCM is capable of providing a variety of imaging modes, swaths, and polarizations with 3–100 m spatial resolution for various applications, (e.g., ship, ice, and oil spill monitoring) [43], [50].

Fig. 2 illustrates examples of SAR images from different instruments discussed above. Moreover, the properties of the most widely used spaceborne SAR systems for oceanographic applications are summarized in Table I. In addition, several missions which have been planned for future years are listed in Table I. Their lifespan Gantt chart is demonstrated in Fig. 3.

B. *Airborne SAR Systems*

In addition to the spaceborne SAR systems that were previously discussed, airborne SAR instruments also provide valuable data for various oceanographic applications. Airborne SAR systems have been widely used to test new technologies and imaging modes and evaluate new RS applications [51].

The main advantage of airborne SAR systems is their flexibility in data acquisition specifications in terms of the look angles and directions, time and location of the data acquisition, revisit time, and many other parameters that can be defined and applied according to a particular application and location [52], [53]. However, airborne SAR systems are more susceptible to imaging geometry distortions. Variations in the velocity and altitude of the aircraft, besides the environmental conditions, complicates the geometry of the airborne SAR systems [53].

Furthermore, because of the relatively low altitude, airborne SAR systems use a wide range of incident angles to obtain moderately wide swaths, and increase the geometry problems. However, due to their high altitude, spaceborne sensors can achieve considerably wide swaths with a much smaller range of incident angles. Moreover, spaceborne systems provide a more consistent imaging geometry and cover a larger area.

Many airborne SAR systems have been developed for acquiring SAR images with various characteristics. For example,

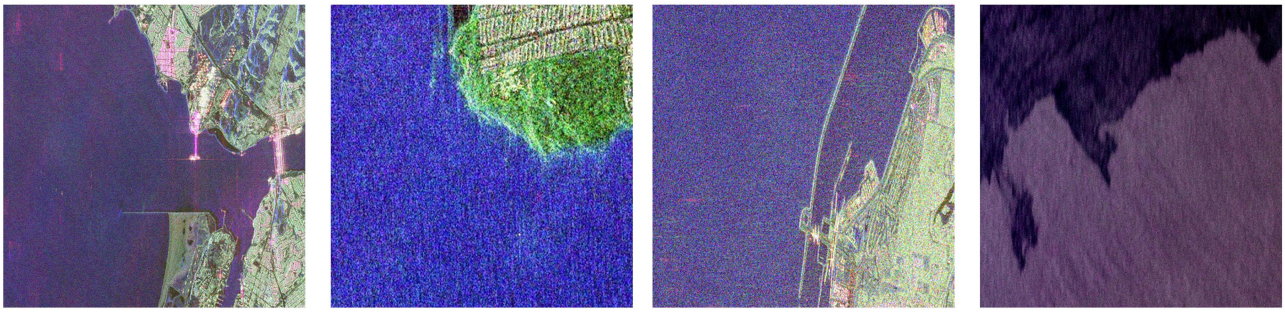

(a) (b) (c) (d)

Fig. 2. Examples of the Pauli RGB composite of SAR images from different sensors. (a) PALSAR-2 onboard ALOS-2 over San Pablo bay, California, the USA with L-band frequency, and StripMap (SM) mode. (b) gaofen-3 over San Francisco bay, California, the USA with C-band frequency, and quad-polarization strip I (QPSI) mode. (c) RADARSAT-2 over Flevoland, The Netherlands with C-band frequency, and fine quad polarization mode. (d) UAVSAR over gulf of Mexico, the USA, during the deep water horizon oil spill incident, with L-band, and PolSAR mode.

TABLE I
LIST OF SPACEBORNE SAR IMAGING SYSTEMS USED FOR OCEANOGRAPHIC APPLICATIONS

Satellite	Sensor	Temporal Res (Day)	Spatial Res (m)	Channels (E.G., Frequency Range)	Ocean Variables (Applications)	Time Period Available	Other Information
SeaSat-1	SAR	–	25	L-band	Oil spill, sea ice, wind speed, dominant wave direction	June – October 1978	First SAR in space
SIR-A	SAR	–	40	L-band		1981	Flew on shuttle missions
SIR-B	SAR	–	20	L-band		1984	Flew on shuttle missions
Resurs-O1-1	SAR-Travers	180	20	L & S-band	Ocean and land, especially for soil moisture	1985-1986	
Almaz-T	Ekor-A1		10–15	S-band		1987-1989	
ERS-1	AMI-SCAT	3–35	30	C-band	Sea ice, wave direction	1991-2000	
JERS-1	SAR	44	18	L-band		1992-1998	Both optical and SAR instruments
SIR-C/X-SAR	C / X-SAR	–	< 30	L, C, and X-band		1994	Flew on shuttle missions
ERS-2	AMI-SCAT	3–35	30	C-band	Sea ice, wave direction	1995-2011	
RADARSAT-1	SAR	1–7	10–100	C-band	Sea surface, sea ice, oil spill, wave	1995-2013	
Envisat	ASAR	5	30 – 1 km	C-band		2002-2012	
ALOS	PALSAR	14	7–100	L-band	Ocean surface	2006-2011	
COSMO-Skymed (CSK)	SAR-2000	14 (less than 12 hours revisit for target area)	1–100	X-band	Sea ice, ocean wave patterns, sea current	CSK-1 (2007 - 2020) CSK-2 (2007 - 2020) CSK-3 (2008 - 2020) CSK-4 (2010 - 2020)	Constellation of 4 SAR satellites

TABLE I
(CONTINUE)

RADARSAT-2	SAR	1–4	3–100	C-band	Sea surface, sea ice, oil spill, wave	2007-present	
TSX (TerraSAR-X)	SAR-X	2.5	1–16	X-band		2007-2020	The first X-band sensor on a satellite in space
RISAT-2	SAR-X	–	1–8	X-band	Ship Detection, sea ice	2009-2020	Determined by strategic pointing
TanDEM-X	SAR-X	2.5	1–16	X-band	Interferometric data	2010-2020	TerraSAR program
RISAT-1	SAR-C	30	1–50	C-band	Sea ice, coastal monitoring	2012-2017	
Kompsat 5	COSI	–	1–20	X-band	Oil spill, sea ice	2013-2020	Determined by strategic pointing
Kondor-E	SAR-10	–	1–30	S-band	Military surveillance and civilian hydrology	2013-2014	Determined by strategic pointing
Kondor-E1	SAR-10	–	1–30	S-band	Military surveillance and civilian hydrology	2014-2019	Determined by strategic pointing
ALOS-2	PALSAR-2	14	1–100	L-band	Ocean surface	2014-2020	
Sentinel-1A	SAR	12	4–80	C-band		2014-present	Two satellite constellations have 2 days revisit time
Sentinel-1B	SAR	12	4–80	C-band		2016-present	Sentinel-1A complement
Gaofen-3	SAR-C	7	1	C-band	Sea wave, sea ice, oil spill	2016-present	
ASNARO-2	XSAR	30–150	1–16	X-band		2018-present	Aimed at small-satellite SAR imagery
SAOCOM-1A	SAR-L	8 days (constellation) 16 days (one satellite)	10–100	L-band	Hydrology, ocean observation	2018-present	Argentina's first Remote Sensing mission
SEOSAR (PAZ)	SAR-X	–	1–15	X-band	Wave direction, oil spill, sea ice	2018-Present	Determined by strategic pointing
NovaSAR-S	S-SAR	1 year	6–30	S-band	Soil moisture and biomass	2018-Present	Demonstrating SAR on a mini-satellite
ICEYE	ICEYE SAR	30 (Daily coverage for the full constellation)	1–15	X-band	Ocean, sea ice, and disaster monitoring	2018-Present	Constellation of 18 micro-satellites
Capella	Capella SAR	7	>0.3	X-band	Ocean, sea ice, and disaster monitoring	2018-Present	Constellation of 36 micro-satellites
Gaofen-12	SAR-C	7	1	C-band	Sea wave, sea ice, oil spill	2019-present	

TABLE I
(CONTINUE)

RadarSat Constellation Mission	SAR-RCM	1-4	3-100	C-band	Oil spill, Sea ice, sea surface	2019-present	
RISAT-2B	SAR-X	–	1–8	X-band	Ship detection, sea ice	2019-present	Determined by strategic pointing
RISAT-2BR1	SAR-X	–	1–8	X-band	Ship Detection, sea ice	2019-present	Determined by strategic pointing
RISAT-2BR2 (EOS 01)	SAR-X	–	1–8	X-band	Ship Detection, sea ice	2020-present	Determined by strategic pointing
SAOCOM-1B	SAR-L	8 days (constellation) 16 days (one satellite)	10– 100	L-band	Hydrology, ocean observation	2020-present	
Gaofen-12-02	SAR-C	7	1	C-band	Sea wave, sea ice, oil spill	2021-present	
RISAT-1A (EOS 04)	SAR-C	30	1–50	C-band	Sea ice, ocean topography/currents	Planned (2021)	
Hai Yang 3 (HY-3) A&B	W-SAR	45	1–10	X-band	Land and ocean features	Planned (2021)	HY-3C/D also are planned for 2024/2025
SAOCOM-2 A&B	SAR-L	8 days (constellation) 16 days (one satellite)	10–100	L-band	Hydrology, ocean observation	Planned (2021)	Constellation of 2 Satellites
Kompsat 6	COSI	–	1–20	X-band	Oil spill, sea ice	Planned (2021)	Determined by strategic pointing
ALOS-4	PALSAR-3	7	1–25	L-band	Ocean surface	Planned (2022)	
Sentinel-1C	SAR-C	5 (‘Extra-wide swath’ mode)	4–80	C-band		Planned (2022)	Sentinel-1A complement
NISAR	SAR-L SAR-S	12	2–7	L & S-band	Ice-sheets, ocean surface	Planned (2023)	NASA-ISRO SAR mission
Sentinel-1D	SAR-C	5 (‘Extra-wide swath’ mode)	4–80	C-band		Planned (2023)	Sentinel-1A complement
BIOMASS	SAR-P	25	50–60	P-band	Forest biomass, flooded forest, land and glacier topography	Planned (2023)	
Tandem-L	L-SAR	4	7	L-band	Interferometric data	Planned (2024)	TerraSAR program
HRWS-SAR	HRWS-SAR	2	0.25–25	X-band	Ocean surface, ice	Planned (2026)	TerraSAR program

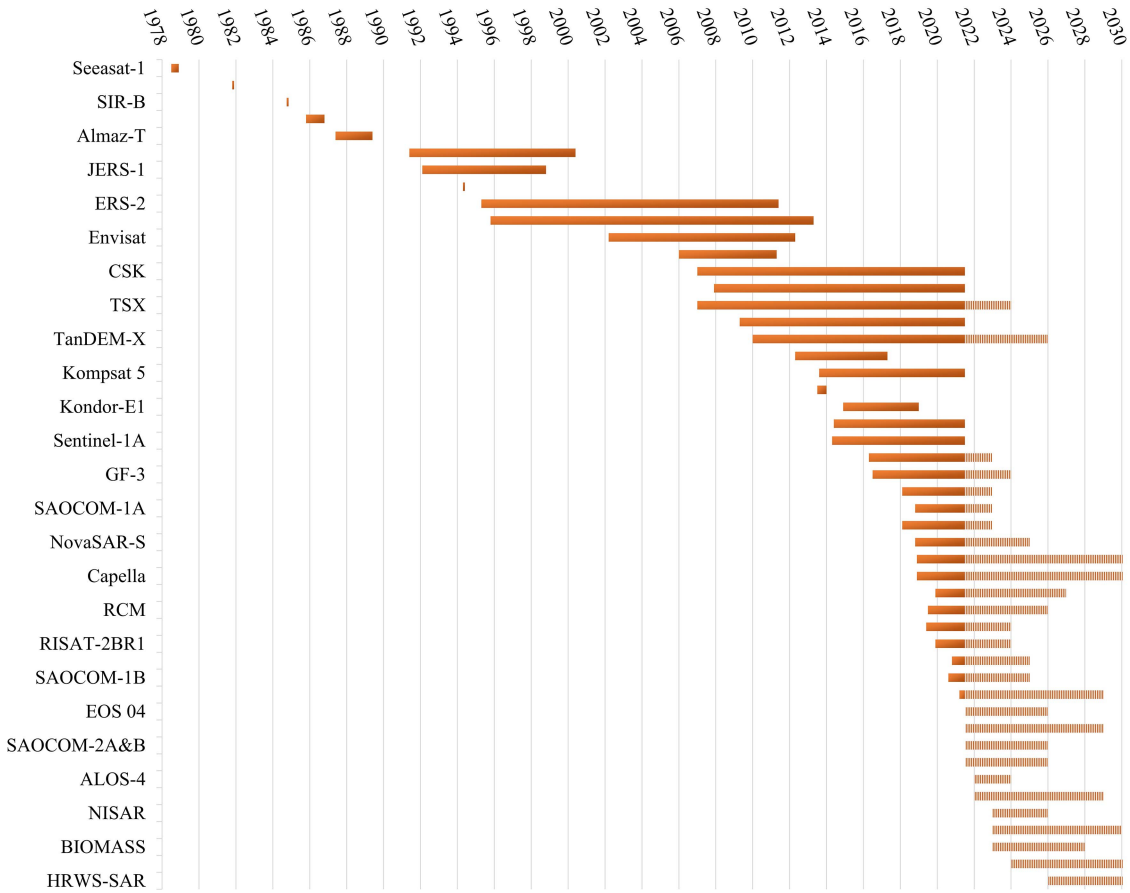

Fig. 3. Lifespan Gantt chart of the spaceborne SAR missions. The period colored with hatches is the expected life time/launch date for the missions.

AirSAR [54], [55] is a multifrequency, multipolarization airborne SAR system with the capability of data acquisition in C-, L-, and P-bands, developed and operated by the Jet Propulsion Laboratory (JPL) of NASA. The spatial resolution of AirSAR imagery is 12 m in both azimuth and range direction, and the incident angles vary between near nadir (near zero) and 70 degrees in the near and far ranges, respectively. UAVSAR [53], [56] is another airborne SAR system that has been developed by the JPL. UAVSAR will eventually be mounted on an uninhabited aerial vehicle (UAV), but currently, it is being operated with a NASA Gulfstream III aircraft. UAVSAR acquires data in fully polarimetric mode with L-band frequency, and the spatial resolution and swath width are 1.8 m and 16 km, respectively.

F-SAR [57] is another well-known airborne SAR system that has been developed by the Microwaves and Radar Institute of DLR. F-SAR acquires fully polarimetric SAR data in X-, C-, S-, L-, and P-bands and was developed after the success of the E-SAR airborne SAR system. Moreover, Polarimetric and interferometric SAR2 (Pi-SAR2) [58] was developed by the National Institute of Information and Communications Technology of Japan after the success of Pi-SAR. Pi-SAR2 provides fully polarimetric SAR images in X-band with a spatial resolution of 0.3 m. In addition to the mentioned airborne systems, there are many other SAR instruments, including the Geographic Synthetic Aperture Radar, EcoSAR, Convair-580 C/X SAR, MicroASAR, and SlimSAR, which have been efficiently employed for ocean applications.

IV. SAR Applications in Oceans

Airborne SAR instruments have provided valuable data for studying ocean surface and internal waves since the 1960s [32], [59]. However, the launch of the SeaSat-1 in 1978 provided data from currents and eddies and other ocean features over a wide range of scales, temperature fronts, shoaling bathymetry, atmospheric patterns related to the storms, roll vortices, and rain cells [32], [59]. SAR data have been utilized for many different oceanographic applications since then [60], [61]. Fig. 4 illustrates the main applications of SAR systems in the ocean, the details of which are discussed in the following sections.

A. Ocean Surface Wind

Ocean surface winds play an important role in transferring momentum, gases, and latent heat between the atmosphere and the ocean [62]. Although scatterometers traditionally have been used for wind retrieval [63], the higher spatial resolution of SAR images has attracted many interests for wind retrievals from SAR images [62], [64]. Moreover, scatterometer measurements can get contaminated by land reflections in coastal regions [65], [66].

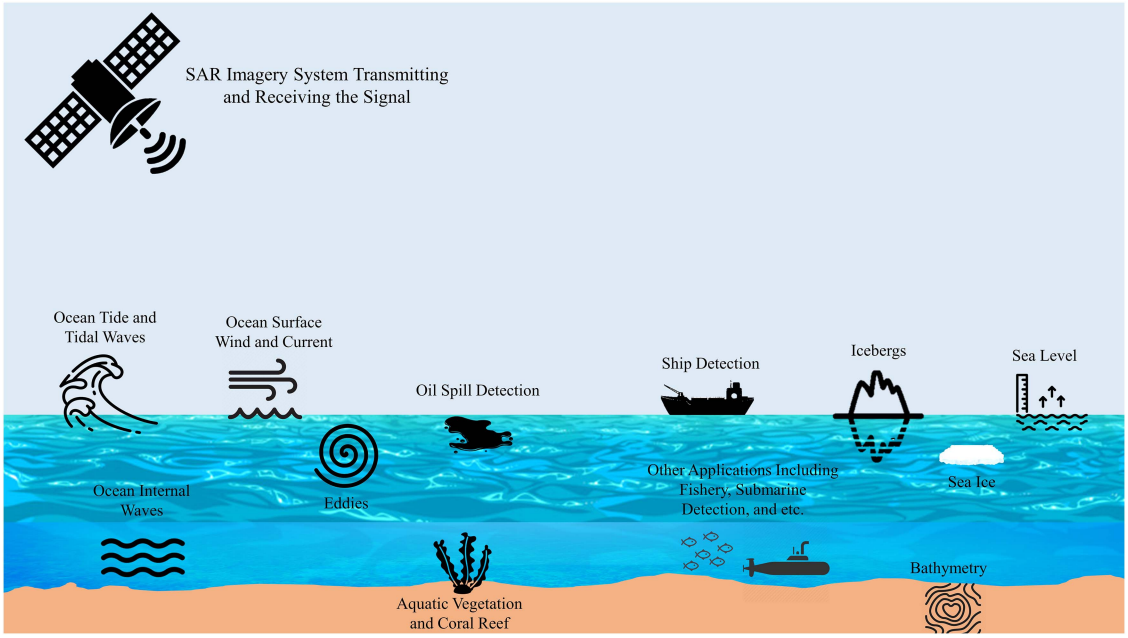

Fig. 4. Overview of different oceanographic applications of SAR systems.

Various approaches have been developed for wind speed and direction estimation from SAR data. In this regard, scatterometry-based approaches are the most widely used techniques for wind speed retrieval from SAR images [64]. These techniques express the relationship between the normalized radar cross-section (NRCS) of SAR data, the geometry of observation, and wind speed through different geophysical model functions (GMFs) [62], [64]. Alternatively, ocean surface wind speed can be derived from SAR images through various techniques, including polarization ratio conversion [67], Azimuth cut-off method [68], neural network-based methods [69], and physical models [62].

Wind direction is another important component of the ocean surface wind that can be retrieved from SAR images. There are many different techniques for this purpose [70]. The fast fourier transform (FFT)-based methods, which computes the Fourier spectrum of SAR image and locates the main spectral energy perpendicular to the wind streaks orientation, is one of the most common approaches for wind direction measurements from SAR images [64], [70], [71]. The main disadvantage of FFT-based methods is the 180° directional ambiguity of the wind direction [64]. Alternatively, wind direction can be estimated through local gradient methods [72], [73], GMFs [66], [74], [75], [76], wavelet analysis [70], and inter-look cross-spectra [77]. Fig. 5 shows the Hurricane Dorian on Sentinel-1 Interferometric Wide swath mode 'VH-polarization image and the wind speed retrievals [78].

Many studies have utilized SAR data for ocean surface wind speed/direction estimation. For example, Fang et al. [9] investigated the effects of the ocean currents on the retrieved SAR ocean surface wind fields. A total of 168 fully polarimetric SAR images, acquired by RADARSAT-2 fine quad-pol mode, were used. The wind vectors were derived from the SAR data using ocean backscatter in cross and co-polarized channels.

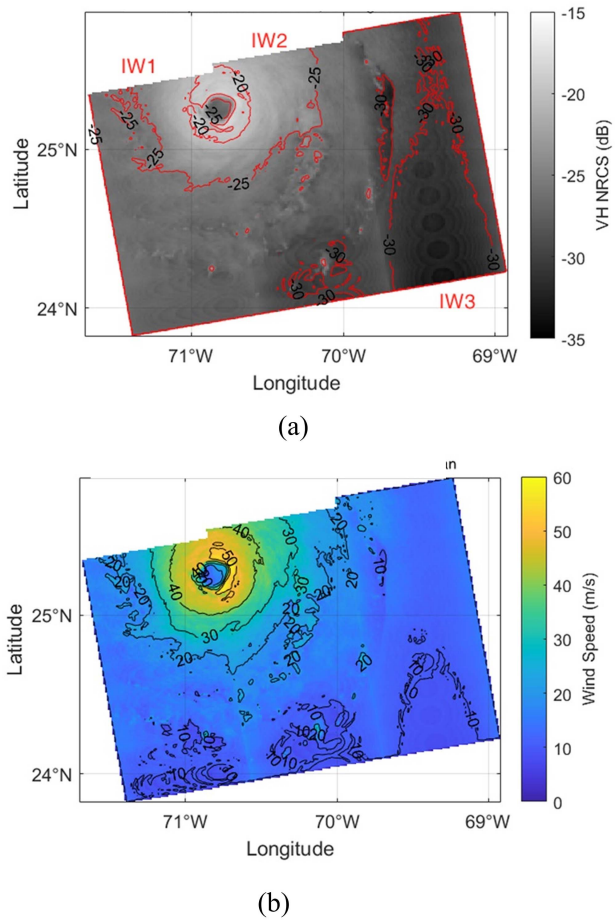

Fig. 5. (a) Sentinel-1 Interferometric wide (IW) swath mode 'VH-polarization image of hurricane Dorian acquired at 22:46 UTC August 30, 2019. (b) Wind speed retrievals of Hurricane Dorian by [78].

In addition, buoy measurements of ocean surface wind and high-frequency (HF) radar measurements were used for comparison. The results illustrated that taking the ocean currents into account could considerably improve the accuracy of wind speed/direction derived from SAR data. In another study, Fang et al. [17] studied the effects of the resampling spatial resolution on ocean surface wind speed retrieval from SAR images. Along with 358 RADARSAT-2 fine-beam quad-polarized SAR images, in situ National Data Buoy Centre and China State Oceanic Administration buoy measurements were utilized in this study. The analysis of the obtained results demonstrated that better accuracy for wind speed retrieval could be obtained at coarser resolutions. Moreover, Zhou et al. [73] have proposed an improved local gradient (LG) model for sea surface wind retrieval from SAR images acquired by the ASAR instrument onboard of the Envisat. In their improved LG method, the smoothing step and computation of the local gradients were combined in the frequency domain. The results were compared with those of the traditional LG and 2-D FFT methods by interpolating wind directions from the European Centre for Medium-Range Weather Forecast (ECMWF) reanalysis data and the cross-calibrated multiplatform wind vector products. The improved LG method demonstrated better performance in terms of sensitivity to different noises.

B. Ocean Surface Current

Ocean surface currents are essential for various met-ocean applications, including studying the ocean and atmosphere interactions, global climate balance, and weather forecasting [9], [10]. Many researchers have suggested using the Doppler shift of the SAR images to estimate the ocean surface currents [79], [80], [81], [82]. The Doppler shift of the backscattered SAR signal can be measured through the difference between the Doppler centroid of the SAR data and the nominal Doppler centroid calculated using the trajectory parameters of the satellite orbit [83]. Furthermore, the wave component should be extracted from the Doppler shift to improve accuracy in ocean surface current estimation [84], [85]. It is worth noting that there is a two-way relationship between ocean surface wind and current [10] and, thus, considering them together in studies of ocean surface parameters would result in a better accuracy [10]. Fig. 6 represents the surface current fields and intensities of the radial components, computed by the Ocean model in [86] for the 0 to 3 m surface water layer depth at the time September 22, 2010, 20:00 and 21:00 UTC.

Many studies have investigated the applications of SAR images for ocean surface current estimation. For instance, Qazi et al. [87] investigated the application of the maximum cross-correlation (MCC) method for ocean surface current studies. Instead of using a few images, a dataset of nearly two years of available sequential SAR images acquired in C-band by the Envisat ASAR and ERS-2 satellites over the coastal California Current System were utilized. The results were compared with the HF radar measurements. It was observed that the current vectors derived from the MCC SAR method had a slightly larger magnitude and were oriented slightly counterclockwise relative

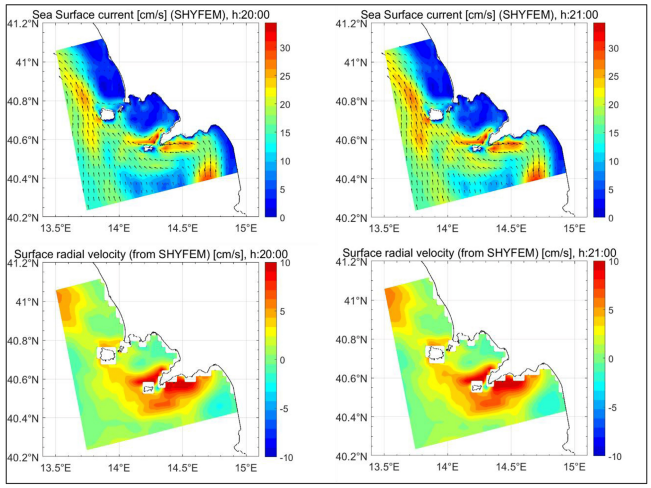

Fig. 6. Surface current fields (upper panels) and intensities of the radial components (lower panels), computed by the Ocean model in [86] for the 0 to 3 m surface water layer depth at the time September 22, 2010, 20:00 and 21:00 UTC.

to HF radar vectors. This might be because HF radar signals penetrate deeper into the water than those of the SAR systems. In addition, Li et al. [88] suggested that measurement accuracy and error analysis of the multiaperture along-track interferometric (MA-ATI) SAR for ocean current vector detection should be done theoretically since the real experimental data for measurement validation is scarce. They considered the main principles of the ocean current measurement of MA-ATI SAR and investigated the accuracy and error simulation model. Moreover, the influences of the SAR parameters and ocean environment of the current vector estimation were investigated. In another study, Sletten et al. [89] carried out experimental investigations of ocean surface current measurement with an ultrahigh-frequency SAR with the ATI mode. Two different approaches for ocean current measurement were described in this study. The first approach was the standard ATI-SAR processing. In the second approach, the ocean surface current was estimated according to the wave energy displacement from the theoretical surface wave dispersion.

C. Sea Level

Sea level is rising globally, and its rate is accelerating [90]. Even small increments in the sea level can cause many problems, especially for people living along the coast. Sea level rise is associated with both climate-related phenomena, including global warming, and nonclimate-related phenomena, such as land subsidence in coastal areas [20]. Hundreds of gigatons of meltwater are being added to the oceans from melted glaciers and ice sheets every year, and the waters in the ocean are expanding by absorbing the heat from the atmosphere because of the greenhouse gasses [20].

Most of the research on sea level rise monitoring using satellite data have focused on SAR altimeters, such as Sentinel-3 [91]. However, SAR imagery has also been applied for relative sea

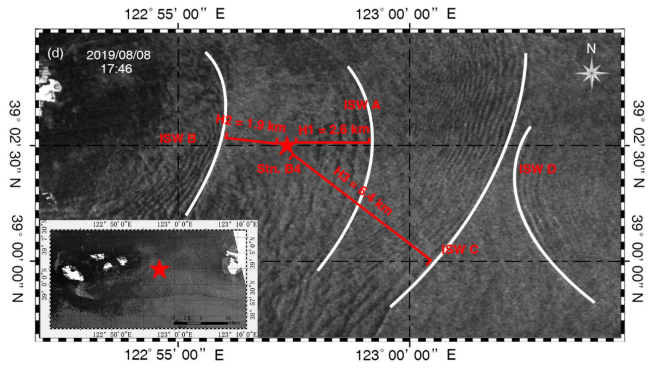

Fig. 7. Internal solitary waves (ISW) on SAR images appear as dark and light strips on the gray ocean surface background [99]. The red star denotes mooring station.

level rise monitoring in coastal regions. To this end, interferometric SAR (InSAR) techniques for land subsidence measurement have been employed [20], [92]. For instance, Gruber et al. [93] used Sentinel-1 SAR images to monitor sea level by connecting the existing tide gauges with the global geometric and physical height reference networks. In this technique, the 3-D geodetic SAR positioning, utilizing Sentinel-1 SAR images, was applied to continuously observe the ellipsoidal coordinates of the tide gauge stations and densify the existing permanent global navigation satellite system (GNSS) networks, which can later be used to connect the height systems across the oceans. In another study, Raucoules et al. [94] proposed a method to estimate local water level variations based on the floating objects on SAR multitemporal data. The range and azimuth offsets of the COSMO-SkyMed multitemporal SAR data were also used in this study to detect the displacement signatures.

D. Ocean Internal Waves

The ocean water column is not homogeneous and has different layers with different density, temperature, and salinity values [95], [96]. Ocean internal waves can happen between those layers and are generated when the interface between the layers is disturbed by ocean storms, strong tidal currents flowing over sharply varying bottom topography, heat exchange, etc. [97]. Studying those internal waves and monitoring various characteristics are very pivotal because they can affect acoustic wave propagation, nutrient mixing in the euphotic zone, sediment resuspension, cross-shore pollutant transport, and human-related activities, including submarine navigation, coastal engineering, and oil exploration [95], [96], [98].

Internal waves affect the surface roughness of the ocean, which can be detected by SAR images [7], [95]. The internal waves interact with the Bragg waves of the ocean surface and increase their amplitude in convergent flow and decrease in divergent flow regions, which increases and decreases the surface roughness, respectively [7], [95]. As a result, the internal waves usually appear as periodically alternating darker and brighter stripes against a gray background in SAR images (see Fig. 7) [96], [99]. The patterns depend on a variety of different factors, including environmental conditions of both the surface and subsurface, as well as the properties of the internal wave itself. The most common pattern is bright and dark band pair combinations; however, many other variations, such as single dark bands and solitary wave interaction patterns (dark "X" shaped features), are also possible [7].

SAR images can be effectively applied to extract different parameters of the internal waves to better understand their behavior and impacts on the environment. These parameters include the number of waves, distance between neighboring waves and wave packets, propagation direction, crest length, and wave speed [95].

Considerable efforts have been made to acquire more accurate data for ocean wave mapping due to the significance of wave information retrieved from SAR instruments. For instance, the Wave mode (WV) measurement of Sentinel-1 was improved compared to those of the Envisat and ERS to have a finer spatial resolution (4 m), higher signal-to-noise ratio, larger scene footprint (20 $\times$ 20 km), and better global sampling. The main advantage of the Sentinel-1 WV imaging mode is its ability to globally measure high-resolution sea surface roughness. However, a very large amount of data from the Sentinel-1 WV dataset ($\sim$120 k images per month) necessitates automated data processing algorithms [100].

Wan et al. [101] argued that the cooperative observations of SAR satellites could resolve the inherent disadvantage of SAR images for waves observation to some extent. Although there are not enough SAR satellites for acquiring multiple simultaneous observations from the ocean to obtain multiview SAR ocean wave synchronization data, the results from simulated Multiview SAR data have demonstrated that the proposed method could effectively compensate for the azimuth cutoff. The simulated synchronized SAR data were in X-band, 4 m resolution, StripMap mode, and single look complex format. The Max Planck Institute (MPI) method was used to obtain the optimum wave spectrum. Huang and Li [102] also used ten years of ASAR WV data to demonstrate the application of WV data for ocean wave measurements. The MPI method was used to derive the 2-D wave spectra from WV data and, subsequently, sea state parameters [e.g., significant wave height (SWH) and mean wave period] were calculated by integrating the 2-D wave spectra. Finally, the results were compared with buoy measurements and demonstrated the applicability of WV SAR data for ocean wave monitoring. Moreover, Gao et al. [15] proposed a new approach for estimating SWH from WV SAR data using the support vector machine (SVM) regression model. In their model, the feature parameters of the SAR image (e.g., sigma naught, the variance of the normalized SAR image, and SAR image spectrum spectral decomposition parameters) were used as the input, and a nonlinear relationship between them and the ocean wave SWH was established. SWH provided by the ECMWF and the buoy measurements were used as the reference data for comparison. The results demonstrated the effectiveness of the SVM model for SWH retrieval from WV SAR images. Collins et al. [103] demonstrated the better performance of a single-layer feed-forward neural network using buoy observations and RADARSAT-2 Fine Quad image data as

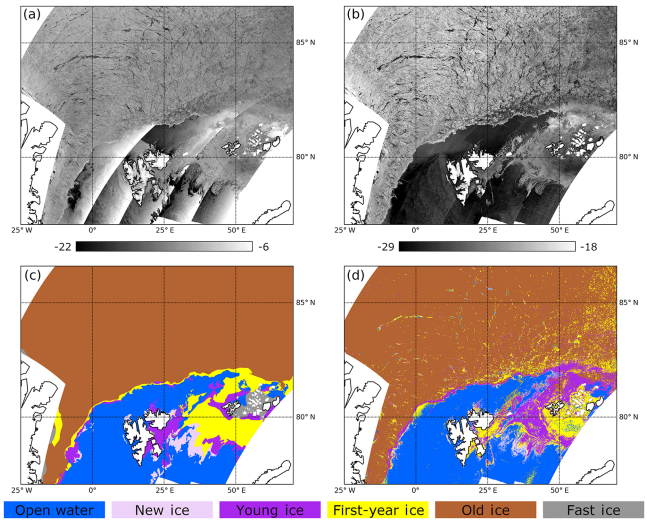

Fig. 8. Sea Ice on Sentinel-1 images with (a) HH and (b) HV polarizations on February 5, 2019, (c) ice classification result. and (d) the weekly ice chart from February 5, 2019 [110].

model inputs for SWH measurement than the CWAVE algorithm using linear regression, with elastic net term selection. They also explored the effect of incidence angle and polarization on the model performance.

E. Sea Ice

Sea ice covers a large portion of the polar oceans and has a significant role in the global weather and climate system. Sea ice influences the exchange of heat, momentum, and matter between the ocean and the atmosphere, solar albedo, and circulations of the oceans [104]. Sea ice coverage and its condition are very important for ship navigation, fisheries, polar and climate studies, and many other offshore activities [104], [105]. Consequently, sea ice monitoring is important for preserving vulnerable polar regions and supporting decision-makers in ocean environments.

Various characteristics of sea ice, including ice coverage, thickness, ice charts, ice surface (roughness), shape and orientation, snow cover, and wetness, can be directly/indirectly derived from SAR images [106]. Generally, co-polarized channel of SAR images provides more informative data for ice analysis [107], and co- and cross-polarized ratios have been proved to be very useful for water and ice types discrimination [108]. Moreover, compact polarimetric SAR data showed promising performance for sea ice classification [109]. Fig. 8 illustrates an example of sea ice on SAR images with HH and HV polarizations, ice classification results from [110] and the weekly ice charts for the same area.

Sea ice mapping and monitoring have been among the most important applications of satellite-based SAR systems since the launch of the SeaSat-1 [105]. Different methods, including thresholding [105], [111], knowledge-based solutions with the use of knowledge and experiences of the ice experts [105], edge detection techniques [105], classification algorithms [112], [113], fully polarimetric parameters-based methods [114], neural network-based methods [115], [116], decomposition techniques [117], textural and statistical analysis [118], and wavelet transform [119] have been developed for this purpose. For example, Ressel et al. [108] utilized HH-VV dual-polarization StripMap images acquired by TerraSAR-X for automatic sea ice classification. In total, 12 different polarimetric features were extracted from the SAR images, and a neural network was trained for pixel-based classification of sea ice. It was reported that some polarimetric features, such as polarimetric span and geometric intensity, were more helpful than eigenvalue decomposition-based features for sea ice classification. Karvonen [115] also utilized both Sentinel-1 SAR images and Advanced Microwave Scanning Radiometer 2 passive microwave radiometer (MWR) data, individually and in combination, to develop and test operational methods for sea ice concentration mapping. Ice concentration grids of the Finnish Meteorological Institute daily ice charts were used as the reference data for the Baltic Sea. The results showed that SAR and MWR data could be solely used for sea ice concentration estimation; however, combined SAR and MWR datasets provided more accurate results, and more details are visible in the combined sea ice concentration maps. Leigh et al. [112] developed an automated ice-water classification algorithm, called MAp-Guided Ice Classification (MAGIC), for dual polarized RADARSAT-2 images. In the MAGIC method, a "glocal" classifier, i.e., a hierarchical region-based classification method based on the published iterative region growing using semantics (IRGS) algorithm, was used for extracting spatial information from SAR images. In addition, the SVM classifier utilized the backscattering and texture features from SAR images for ice-water binary classification. Later, an IRGS was employed to combine the results from the two classifiers and obtain the final ice-water discrimination.

F. Icebergs

The main differences between sea ice and iceberg are that sea ice forms from the salty ocean water and generally forms and melts exclusively in the ocean, while icebergs form from fresh water and snow on land [120]. Accurate and consistent monitoring of icebergs globally is crucial for various reasons, such as safe navigation of the ships. Icebergs and glaciers have the potential to influence global sea level, ocean currents' circulation, water salinity, and sea ice formation [121], [122].

Although various satellites have been utilized for iceberg studies, they have different limitations. For example, the low spatial resolution of the scatterometers limits monitoring small icebergs. Deformed sea ice causes various problems for radar altimetry. Optical satellites are also restricted by darkness and cloudy condition, besides the difficulty in distinguishing between snow and ice [121], [123]. However, SAR satellite imagery provides more valuable data with a high spatial resolution and almost under all weather conditions. Fig. 9 shows A-72 and A-73 icebergs on Sentinel-1 image acquired on January 19, 2021 [124].

Icebergs usually have higher backscattered intensity than the surrounding regions and are characterized by both surface and volume scattering mechanisms [121]. As a result of the higher intensity, many researchers have utilized band thresholding,

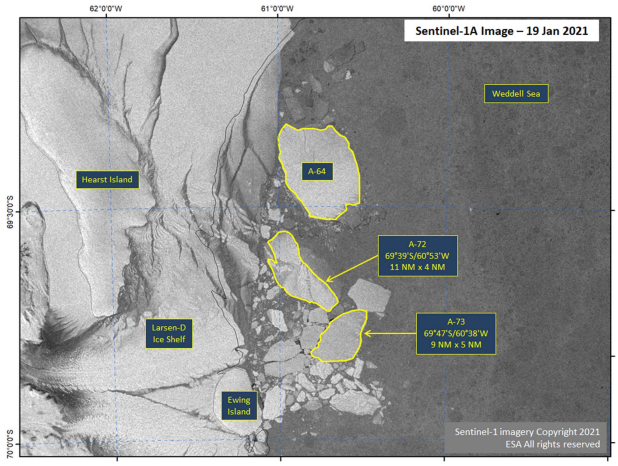

Fig. 9. A-72 and A-73 icebergs on Sentinel-1 image acquired on January 19, 2021 [124].

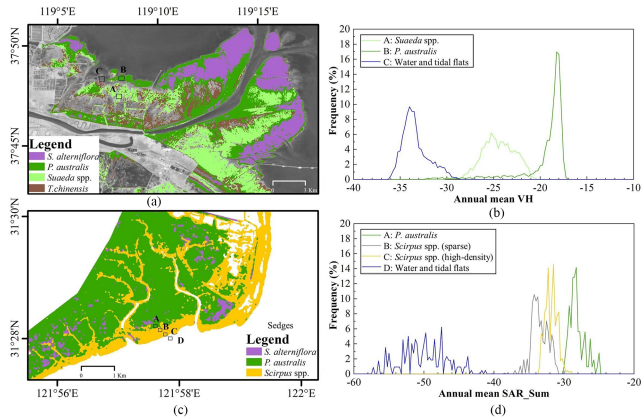

Fig. 10. Classification of different salt march samples from SAR features for (a) Yellow river estuary with the (b) annual mean composite VH features of the scene, and for (c) Yangtze river estuary with the (d) annual mean SAR sum features [134].

including adaptive threshold techniques, for iceberg detection on SAR images [125], [126]. However, such algorithms do not provide satisfactory results when the contrast is small (e.g., in windy and rough sea surface conditions) [121]. Furthermore, differential interferometric SAR (DInSAR) technique is useful for mapping the ice sheet grounding line (i.e., the line where the ice detaches from the ground, and becomes afloat on the ocean) [127]. Various classification methods have also been proposed for iceberg detection, considering the edges between different backscattering coefficients [121], [128], [129]. Due to the recent advancements and promising results of the neural networks and deep networks, many researchers have focused on applying those methods to iceberg detection using SAR images [18], [129]. However, automatic discrimination between icebergs and ships, which conventionally has been done by manual detection and human interpretation, is still a challenge [18].

Hass and Arsanjani [18] proposed a deep learning method based on the YoloV3 framework for discriminating between ships and icebergs in SAR images. Dual polarized Sentinel-1 SAR images acquired over Greenland were used in this study. The main focus of this study was on highlighting the challenges in implementing and validating the deep learning approaches for iceberg and ship discrimination in SAR images. It was demonstrated that the lack of high-quality and large-scale annotated dataset was the most prominent problem in this field, and future studies should work in annotating suitable datasets, as well as developing state-of-the-art algorithms. In another study on the applications of neural networks for ship-iceberg discrimination in SAR images, Bentes et al. [130] utilized a convolutional neural network (CNN) model for ship-iceberg discrimination in high-resolution SAR images acquired by TerraSAR-X StripMap mode. In order to balance the number of the samples per class and avoid overfitting of the model, 277 and 68 samples of ships and icebergs, respectively, were extracted from the multi look ground range detected SAR products. The extracted samples were used for data augmentation and creating a balanced dataset consisting of 600 samples. Comparing the results with those obtained from the SVM classifier showed that the CNN was capable of learning more relevant features from the input images and obtained better generalization. However, the SVM algorithm was trained faster and with less computational effort. In addition, Mazur et al. [121] proposed an automatic object-based method for iceberg detection from ASAR images in the Amundsen Sea, Antarctica, under cold temperatures and hard winds. They used brightness and spatial parameters of the ASAR images at five scale levels for iceberg detection and verified the results with the Level-1B imagery from NASA's Operation IceBridge mission in 2011, and manual classification results.

G. Aquatic Vegetation and Coral Reef

Aquatic vegetation and coral reefs have significant ecological functions in the marine ecosystem. They produce oxygen and provide habitat and food for fish, crabs, and other aquatic organisms. Yet, they are very vulnerable to coastal development and water quality degradation [131]. Although most of the studies about aquatic vegetation and coral reef mapping and monitoring using satellite data have focused on multispectral imagery [132], a significant correlation has been proved between the SAR backscattering coefficient and both above-water dry biomass and height of the plants [19]. SAR data can be utilized for mapping coral reef and underwater plants, depending on the sea state and acquisition quality [19], [133]. Fig. 10 demonstrates the distribution of different salt marsh samples from SAR features in (a) Yellow River Estuary and (b) Yangtze River Estuary [134].

Coral reef and aquatic vegetation are indirectly detectable in SAR images due to the interaction of the water currents with the underwater features, which modulates the sea surface roughness and the interaction of the radar wave with the sea surface [19], [133]. Most of the studies on aquatic vegetation monitoring through SAR data combined field campaign data with SAR backscattering coefficient to map above- and underwater plants to obtain a better accuracy [135]. Various supervised and unsupervised classification algorithms have also been used for aquatic vegetation mapping from SAR images [19], [135]. For instance, Nair et al. [19] investigated the applicability of

RISAT-1 SAR images for coral reefs mapping in Andaman and Lakshadweep Islands in the Indian Ocean. Preprocessing steps, including the land mask and speckle filtering, were applied to the dual-polarized georeferenced RISAT-1 SAR images. Finally, the ISODATA unsupervised classification algorithm was used for classification and delineating the coral reef areas. Moreover, Costa et al. [136] combined SAR images and field measurements to estimate biomass changes and mapping aquatic vegetation in the lower Brazilian Amazon. The correlation between the radar backscatter and both above-water dry biomass and the height of the plants were subsequently analyzed. A logarithmic correlation was detected between the backscattering coefficients and multiple biophysical properties of aquatic vegetations. SAR images from RADARSAT-1 (C-band) and JERS-1 (L-band) were used in this study and the results demonstrated that the C- and L-band SAR images could accurately map aquatic vegetation in the Amazon floodplain. Moreover, Tsyganskaya et al. [137] conducted a thorough review on SAR-based detection of the flooded vegetation. They have analyzed the relevant publications from Web of Science search engine between 1 January 1985 and 26 July 2016. After applying different filters on the Web of Science publications, 128 articles were selected for further analysis. The interaction between the SAR signal and flooded vegetation, as well as the sensor characteristics, environmental parameters, and processing techniques were discussed. It has been concluded that there is a growing demand for unsupervised and computationally efficient methods for flooded vegetation studies.

H. Ship Detection

Ship detection is one of the main tasks for maritime surveillance and security. Ship detection is required for border control, monitoring ocean pollution, safe navigation, and rescue operations [12], [138]. There are several different techniques for ship detection, each of which has its advantages and disadvantages. Due to their unique capabilities, day and night and almost all-weather data acquisition, SAR images are effective sources for ship detection in the ocean [12], [138].

Multiple studies have focused on wake detection to predict the ship's location [139]. However, ship wakes would be invisible from some look angles of the radar, and sea clutter might complicate the wake detection procedure. Therefore, the majority of the researchers have focused on ship detection rather than wake detection [12]. During calm weather conditions (i.e., low wind speed), the ocean surface reflects the majority of the received radar signal in the opposite direction and, thus, the ocean surface appears very dark on the SAR image. However, the double-bounce backscattering mechanism from the ship's body causes a strong backscattered signal and appears as bright targets in the SAR image. On the other hand, high wind speed and cluttered ocean surfaces brighten the whole SAR image and make the ship detection procedure challenging. This becomes more serious for small ship detection because large waves also cause double-bounce backscattering [12]. Fig. 11 illustrates several marine vessels on a calm water surface, which are detectable in the HV polarization of the ALOS-1 SAR image.

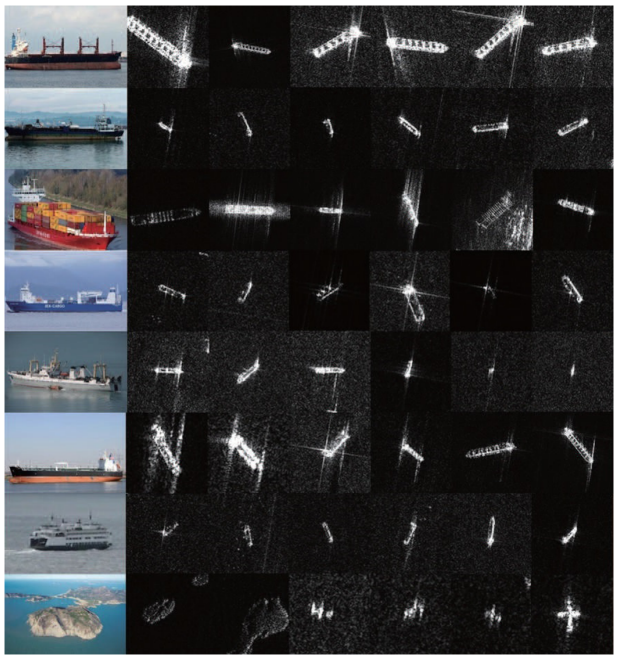

Fig. 11. Examples of the different ships (i.e., bulk carriers, general cargos, containers, other cargos, fishing, tankers, and other ships), as well as the common false alarms for ship detection applications in SAR images [140].

Conventionally, constant false alarm rate (CFAR) methods have been used for ship detection in SAR data [141]. CFAR methods adapt a threshold in the detection window, considering the statistical distribution of the signal on the ocean surface to achieve a given probability of false alarm [12], [141]. Despite the simplicity of the CFAR methods, their detection ability dramatically decreases on cluttered ocean surfaces [12]. Many other algorithms, including wavelet-based methods [142], polarization-based algorithms [143], neural network [144], [145], [146], [147], and human visual attention system-based methods [12], have also been developed for ship detection using SAR images. The accuracy of these methods mainly depends on the contrast between bright targets and dark backgrounds.

Amoon et al. [12] proposed human visual attention system-based models for ship detection in SAR images, and compared their results with those of the CFAR method. They indicated that the human visual attention system always focuses on the most prominent objects, and since the ships are prominent objects in dark SAR images of the oceans, they could be easily identified by their proposed models. Furthermore, Fan et al. [144] designed a segmentation method based on a pixel-wise CNN (i.e., U-Net) for ship detection in compact polarimetric SAR images. In their proposed model, several convolutional down-sampling layers were utilized for feature extraction, and later, up-sampling layers used deep semantic and shallow high-resolution features to classify the images in three semantic classes (i.e., Ship, Land, and Sea). Quad polarization SAR images acquired by Gaofen-3 were used to simulate compact polarimetric SAR images. The proposed method was compared with the standard CFAR and Faster Region-based CNN, and it was observed that their method was more effective, especially in reducing the impact

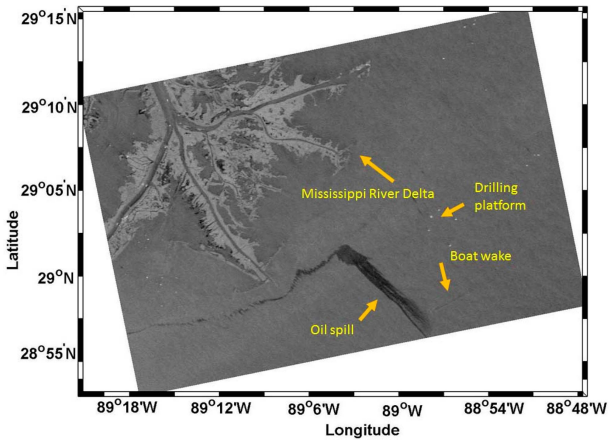

Fig. 12. Example of oil spill on RADARSAT-2 images [158].

of the ocean clutter and SAR ambiguities. Guo et al. [148] also proposed a new model for ship detection in SAR images, called CenterNet++. In this model, a feature refinement module was employed to extract multiscale contextual information to solve the problem of small ship detection in SAR images. Later, a feature pyramids fusion module was utilized to create more powerful semantic features. Finally, a head enhancement module was used to create a balance between the foreground and background to address the problem of the complex background. The proposed model was tested on three datasets (i.e., AIR-SARShip, SSDD, and SAR-Ship) and demonstrated high performance.

I. Ocean Oil Spill Detection

Oil pollution in the ocean is a devastating environmental problem, therefore, immediate detection of oil spills is crucial [149], [150]. SAR has been proved to be an effective tool for oil spill detection and monitoring [11], [151], [152], [153], [154]. Generally, oil spills appear as dark areas on the water surface due to the decreased surface tension and lower NRCS values compared to the surrounding water. Various oil spill detection techniques, such as statistical analysis [155] and classification algorithms [152], [156], [157], [158], have been developed for oils spill detection in SAR images. It has also been reported that the wind speed and SAR imaging incidence angles should be considered for accurate oil spill detection using SAR images [153].

The major problem for oil spill detection using SAR data is other lookalike natural phenomena (e.g., biogenic slicks, upwelling, low wind areas, rain cells, shear zones, and internal waves). In fact, these phenomena also appear dark on the water surface in SAR images [158]. Most of the oil spill detection methods using SAR data have focused on discriminating between the oil spill and other similar targets. For instance, the shape and position of the dark area can be used for this purpose (e.g., narrow oil spill behind the ships) [159]. Moreover, polarimetric features [152], [156], [157], [160] and standard deviation of co-polarized phase difference [151] have been proved to be useful for oil spill detection. Fig. 12 shows an example of the oil spill acquired by RADARSAT-2.

Song et al. [158] demonstrated the superiority of combining multiple polarimetric features of the PolSAR data along with the optimized wavelet neural network (WNN) classifier for ocean oil spill detection. This study used the Jeffreys–Matusita distance to select optimal features for distinguishing different objects, including clearwater, drilling ring, ships, and ship wakes, from the ocean oil spill. Finally, SPAN (backscattered energy), H (polarization entropy), μ (conformity coefficient), P (degree of polarization), and $\bar{\alpha}$ (mean scattering angle) were selected as the best SAR features to be used within the optimized WNN classifier. Two fully polarimetric SAR images acquired by RADARSAT-2 in fine quad-polarization imaging mode over the Gulf of Mexico were used to evaluate the performance of the proposed methodology. The results of the optimized WNN were compared with unoptimized WNN outputs, and it was observed that the optimized WNN could improve the classification accuracy, regardless of the input features. Conceição et al. [161] compared two methods for oil spill detection in Sentinel-1 SAR images. The Random Forest classifier was employed in the first model to classify the SAR images into seven semantic classes, including oil spills, biological films, rain cells, low wind regions, clean sea surface, ships, and terrain. The second model was an oil detector of SAR images called the Radar Image Oil Spill Seeker, which was used to distinguish oil from other targets. The results demonstrated the importance of dataset biases and optimized feature sets for oil spill detection in SAR images. Shaban et al. [162] also proposed a two-stage deep learning framework for oil spill detection in SAR images with a special focus on highly unbalanced datasets. In the first stage, a 23-layer CNN model was employed to classify the patches based on the distribution and percentage of the oil-covered pixels, and in the second stage, a 5-level U-Net was developed for semantic segmentation of the patches which were selected in the first stage. Despite the improved overall performance, the proposed methodology neglected the patches with insignificant oil-covered pixels.

J. Ocean Tide

Gravitational forces of the moon and sun, as well as the Earth's rotation, cause a regular rise and fall in the sea level, referred to as ocean tides [163]. Ocean tides can affect water circulation, ocean currents, marine life, and coastal human activities [164]. Moreover, many small marine organisms, including crabs, snails, and seaweeds, live in tidal zones. The fish concentration also depends on the tidal currents, and the fishery industry uses tidal information for a more efficient fishery [165]. In addition, since the tides affect the sea level in coastal areas, ships should consider them for safe navigation, especially in shallow coastal waters [166]. Ocean tides are also significant for construction projects in coastal areas, and engineers use tidal information. Moreover, tidal currents can play an important role in mixing coastal pollutants with ocean water. Finally, coastal energy can be harvested by installing tidal powerhouses in tidal zones as an immense renewable energy source [167], [168].

Due to the importance of ocean tides, SAR has been utilized for ocean tide studies. For example, InSAR techniques are capable of extracting sea surface parameters with a relatively high resolution and are the most frequently used SAR methods for tidal studies [22], [169]. In addition, waterline, which is an important parameter for tidal studies, can be extracted from SAR data using advanced edge detection methods between the flat tidal zones and rough sea surface [170]. Moreover, phase information in complex-valued SAR data can be utilized for tidal information extraction through analyzing Doppler measurement and signal processing techniques [169]. Fig. 13 shows the empirical displacement maps showing tide-deflection ratio [171].

Many studies have investigated the potential of SAR systems for tidal studies. For example, Han and Lee [164] estimated the tidal deflection of Campbell Glacier Tongue using 120 Double-Differential Interferometric SAR (DDInSAR) images from 16 COSMO-SkyMed one-day tandem DInSAR pair images. A pixel-based linear regression model between the DDInSAR-derived tidal deflection and the tidal variation predicted by various tide models was employed to generate the tide deflection ratio map. The results demonstrated the necessity of continuous acquisition of COSMO-SkyMed one-day tandem DInSAR pairs and their importance for investigating the tidal deflection of fast-flowing glaciers as well as the reliability of the DDInSAR technique for ocean tidal studies. Moreover, Baek and Shum [172] investigated the application of the DInSAR technique with ERS-1/2 tandem data for estimating the tidal constituents underneath the Sulzberger ice shelf, West Antarctica. The InSAR data were corrected for the effects of the atmospheric loading and the tidal constituents were calculated through differentiating the corrected InSAR data. The results were compared with the tidal constituents from a contemporary regional tide model (CATS2008a) and a global tide model (TPXO7.1). The results illustrated the feasibility of estimating tidal constituents from ERS-1/2 SAR observations through the DInSAR technique. Furthermore, Ferreira et al. [169] utilized the ATI-SAR technique for mapping the surface tidal currents and assessment of its tidal energy resources. Different conditions of ATI-SAR imaging scenarios, considering environmental conditions and sensor parameters, were simulated. The results from the ATI-SAR simulations were compared with in situ measurements. It was observed that SAR data and the ATI-SAR technique had a high potential for estimating tidal currents and evaluating their energy resources. This study demonstrated the importance of the ATI-SAR technique for tidal power site assessment and its suitability for identifying potential ocean tidal current energy sites.

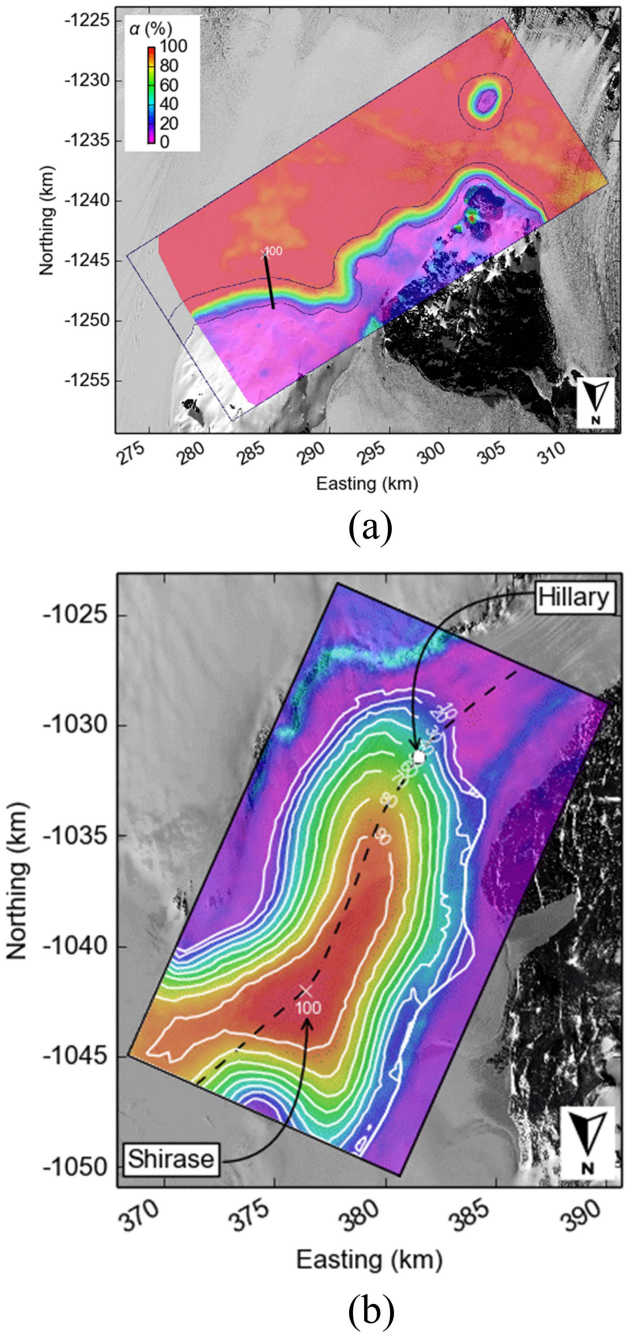

Fig. 13. Empirical displacement maps showing the tide deflection ratio in (a) McMurdo Ice shelf and (b) Darwin Glacier. Tide-model locations and reference points are shown with the white crosses. White contours delineate areas of constant vertical displacement [171].

K. Eddies

An eddy is a circular current of water. Oceanic eddies are important elements of ocean dynamics and play an important role in oceanographic studies. They determine the horizontal mixing of the ocean and influence the biological organisms, distribution of organics, pollution expanding, and the transportation of heat and salt in the ocean [16], [21], [173]. Consequently, studying eddies and their features has always been of interest.

SAR imagery can be efficiently employed for eddies detection and also retrieval of their different parameters, such as rotation direction, horizontal dimensions, spiraling order, eddy asymmetry, and location of surface convergences [16], [174]. The main reason why oceanic eddies become visible in SAR images is that they change the water surface roughness. Generally, they appear in SAR images due to two main mechanisms: the first mechanism is the accumulation of surfactants and surface films in convergent regions where they reduce the sea surface roughness, and the second mechanism is the interaction of

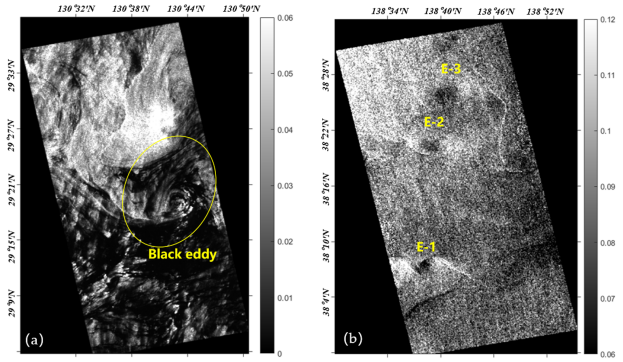

Fig. 14. Tow examples of eddies on ALOS PALSAR VV-polarized backscattering coefficient images, illustrating (a) black, and (b) white eddies [177].

the waves and currents of the ocean [175]. Wind speed is the most important parameter for the main mechanism of oceanic eddies in SAR images [175]. Surface films' accumulation is the main mechanism in low and moderate wind speeds, and eddies usually appear as dark spiral flows. However, surfactant films are disrupted by the wind in higher wind speeds, and the oceanic eddies manifest in SAR images because of the wave and currents interaction and appear as bright curved lines [175]. Fig. 14 demonstrates two examples of eddies on ALOS PALSAR VV-polarized backscattering coefficient images [177].

Du et al. [174] studied the dynamic changes of the ocean eddies caused by complicated ocean environments in SAR images. The proposed method was based on the adaptive weighted multifeature fusion. This algorithm utilized texture, shape, and corner features extracted from the global gray level co-occurrence matrix, detailed Fourier Descriptor, and local salient Harris features, respectively. A multiple kernel learning (MKL) was used for adaptive weighted feature fusion and, finally, an SVM classifier with a combined kernel function was trained for eddy recognition in SAR images. Kozlov et al. [16] also utilized multimission spaceborne SAR images (C-band SAR images from Envisat ASAR and Sentinel-1 SAR-C instruments, and L-band SAR images from ALOS-2 PALSAR-2) over the open ocean and in the marginal ice zones to estimate eddy characteristics in the Western Arctic Ocean. In total, 7749 SAR manifestation of eddies, including 4078 eddies in the open ocean and 3671 eddies in the marginal ice zone and near ice edges, were manually identified through visual inspection of the SAR images at full resolution and exploring different eddy signatures of SAR images. Finally, various inspections were carried out on the results to analyze the eddies' properties of the Western Arctic Ocean. In addition, Karimova and Gade [178] used 1250 SAR images acquired by the Envisat ASAR instrument between 2009 and 2011 over the Baltic Sea to investigate spatio-temporal distribution of submesoscale eddies. Considering the importance of near-surface wind speed for eddies detection in SAR images, wind data from a numerical model was also utilized to enhance the results. Various environmental parameters, including the sea surface temperature, surface currents, and near-surface wind speed, were also analyzed in the regions that eddies were identified to determine the correlation between these parameters and eddies in the Baltic Sea.

L. Bathymetry

Due to the increasing trend in offshore construction activities, the demand for bathymetry and the topography map of the seafloor has considerably increased in the recent years. Although the microwave signal cannot significantly penetrate the water body, SAR is capable of indirectly retrieving bathymetry information through the variations in the small-scale sea surface roughness caused by the shallow sea floor topography [133], [179].

Changes in underwater topography modulate the surface flow, which results in surface wave spectrum variations [179]. Underwater topography and bathymetry techniques from SAR data are based on these surface wave spectrum variations and wave characteristics [133]. The FFT-based methods are the most common approaches for computing directional wave spectra and retrieving the water depth by solving the linear dispersion relation from SAR images [133], [179]. Moreover, swell patterns and the scattering mechanism have also been used for this purpose [180]. For example, Pereira et al. [179] have explored the open-access Sentinel-1 SAR data to estimate nearshore bathymetry using the FFT. This study examined the sensitivity of the estimation of wave characteristics to input parameters, as well as the applications of multitemporal sentinel-1 data for bathymetric studies. The performance of the algorithm was verified through testing with both simulated and real SAR images. The resulting map of the wave characteristics was utilized to generate the bathymetry information through the linear wave theory. Furthermore, Bian et al. [8] employed numerical simulations on four Sentinel-1 SAR images and quantified the sensitivity of the bathymetry results to different initial input parameters, such as wavelength, swell period, and initial water depth. SAR images of different spaceborne missions, including ALOS-2 with L-band, GF-3, RADARSAT-2 and Sentinel-1 with C-band, and TerraSAR-X and COSMO-SkyMed with X-band frequencies, were utilized to calculate the minimum and maximum detectable shallow water depth ranges. The results demonstrated the suitability of linear dispersion relation for estimating coastal bathymetry from SAR satellite imagery. In addition, the sensitivity of the estimated water depth analyses showed that the water depth is the most important parameter in this regard and the TerraSAR-X satellite had the highest water depth detection range. Moreover, Wiehle and Pleskachevsky [181] used TerraSAR-X and Sentinel-1 data to derive bathymetry in coastal sea with the shoaling effect. According to the shoaling effect, the wavelength and height of the waves change while passing the underlying topography. They developed an automatic algorithm to retrieve the peak wavelengths of the long swell waves in SAR images and to calculate the bathymetry based on the shoaling effect. Fig. 15 illustrates their retrieved bathymetry using the TerraSAR-X StripMap scene acquired on March 31, 2010 around the Channel Island of Jersey.

M. Other Applications

In addition to the above-mentioned SAR applications in the ocean, many other oceanographic parameters can be derived from SAR data. For instance, polar mesoscale cyclones and

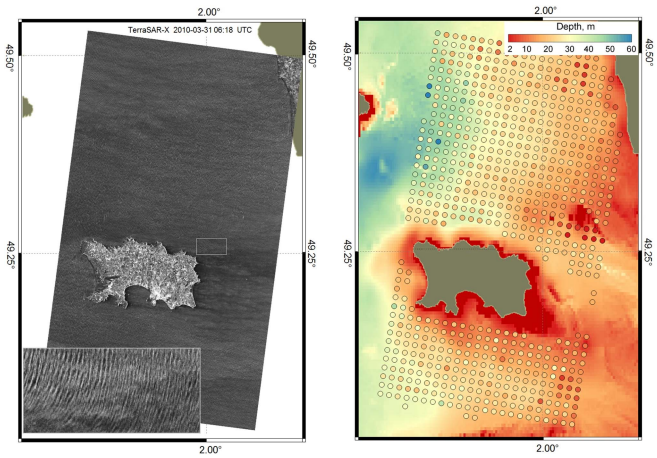

Fig. 15. Bathymetry map retrieved from the TerraSAR-X StripMap scene acquired on March 31, 2010 around the channel island of Jersey through the algorithm presented in [181].

tropical hurricanes can be monitored using SAR images [182], [183]. In this regard, Zhang et al. [182] used 75 RADARSAT-2 ScanSAR images, acquired between 2008 and 2017, to extract the tropical cyclone centers, the radius of maximum winds, intensities, and the azimuthal wave-number one asymmetric surface wind structures. The authors used cross-polarized (VH) SAR images in their study because co-polarized (HH and VV) channels of the SAR images are usually saturated in high winds and are not suitable for monitoring high wind phenomena. Furthermore, a high wind speed hurricane retrieval model [184] was utilized for wind speed and hurricane retrieval. Finally, quantitative analyses on the symmetric mean flow and the asymmetries of azimuthal wave-number one in the surface wind fields were carried out.

Forecasting disasters for early warning purposes is another useful application of SAR imagery [185], [186]. In this regard, Chen et al. [186] proposed a damage index to discriminate urban patches with various damage levels after earthquake and tsunami events in the Kawauchi Campus of Tohoku University, Sendai, Japan, using full polarimetric SAR images,. Co-polarized coherence in the rotation domain along the radar line of sight in multitemporal ALOS-PALSAR PolSAR data was used in the proposed damage index.

Coastline monitoring, especially in sensitive environments such as river deltas, is essential for understanding coastal environments and climate change, which can effectively be investigated using SAR imagery [187], [188]. In this regard, Zhe et al. [188] used multisource, multitemporal, and multiband optical and SAR images to detect dynamic changes of the coastline in the Yellow River delta, northeast of Shandong Province, China, between 1980 and 2020. Various spaceborne optical (Landsat-3, −5, −8), and SAR (Envisat-ASAR, Sentinel-1, and GaoFen-3) images were integrated in this study for coastline change mapping. The morphological operation was applied to the pre-processed SAR images to extract the coastline. Finally, GPS-RTK measurements were used for validation of the results.

Narrow water channels, ships passage, sea ice drift, and arch evolution can also be monitored using SAR imagery [189]. For example, Shokr et al. [189] utilized daily Sentinel-1 SAR images to monitor sea ice drift and arch evolution in the Robeson channel between Greenland and Ellesmere Island in the Arctic. Two mechanisms were investigated in this study. First, the drift speed and direction of individual ice floes were conducted by manual tracking for 39 ice floes. The tracked information was justified by the wind reanalysis data or other factors, such as ocean current, surrounding ice concentration, and tidal forces. Second, the development of the ice arch at the Robeson channel's inlet until its maturity was monitored. Despite being laborious, the manual approach resulted in a satisfactory accuracy.

Internal solitary waves are nonlinear and nonhydrostatic gravity waves that usually form as a result of the interaction between the barotropic tide and steep bottom bathymetry, and propagate along with the density layers of the ocean. Internal solitary waves can have an important role in various oceanographic phenomena and SAR images are very useful to study and monitor them [190]. For instance, Magalhaes et al. [190] used a collection of 32 Sentinel-1 SAR images to study the 2-D horizontal structure of the internal solitary waves between two large submarine canyons on the Western Iberian shelf. In this study, the suitability of SAR data for detecting the potential areas for wave–wave interactions was evaluated. In addition, the energy proxies of the internal solitary waves in the wave–wave interaction fields on the SAR images were compared with the nominal noninteracting background.

Seafood has always been an important source of food for humans, especially in coastal areas. Accurate and real-time information about the location and number of fishes can enhance fishery activities. Moreover, precise legislation and monitoring strategies are necessary to protect sea life and restrain overfishing. SAR systems provide valuable datasets for monitoring fishery activities. For example, Galdelli et al. [191] integrated Sentinel-1 SAR images with the automatic identification system (AIS) data to identify suspicious behaviors and monitor fishing activities. A searching method using the unidentified maritime objects algorithm was used along the Sentinel-1 SAR images to detect the ships. The detected ships were then applied to automatically fill the data gaps in the AIS due to nonreported ship positions that could be because of the technical problems or intentional hiding of the position for illegal activities, including illegal fishing. Moreover, Takasaki et al. [192] combined SAR images and nighttime visible images from the visible infrared imaging radiometer suite data for monitoring fishery activities on the Yamato-Ridge and surrounding areas in the Japan Sea. Combining these two data sources compensated the defects of the SAR images due to not observing small wooden boats in ScanSAR mode, as well as the deficiency of visible/infrared images because of relying on the fishing lights to observe the ships. A matching procedure between the detected ships on both data sources was performed to identify the types of ships (i.e., steel ship with fishing light, wooden ship with fishing light, steel pair-trawler ship with no light, and others).

Finally, many researchers have studied many other oceanographic phenomena using SAR imagery. These include but not limited to sandbanks and shellfish stocks in the sea [193], rainfalls and other atmospheric boundary layer phenomena [194],

TABLE II
ADVANTAGES AND DISADVANTAGES OF SAR SYSTEMS FOR OCEANOGRAPHIC APPLICATIONS

Advantages	Disadvantages
• Almost independent from the weather condition, cloud coverage, and solar illumination • Availability of high spatial resolution data • Applicable to both low and high wind speeds • Image-based measurement • Wide spatial coverage • Imaging with various polarizations and frequencies • Availability of different data acquisition modes • Penetration capability in shallow water and snow • Contains physical properties • Accurate estimation of ocean surface topographic changes • Sensitive to small changes in surface roughness • Applicable to several near-real-time applications	• Reactively intensive pre-processing steps • Requires complicated signal and image processing methods • Complex-valued operators are required for processing complex-valued SAR data • Difficult data interpretation • Presence of speckle noise • Presence of scalloping, foreshortening, and layov er effects • Low accuracy for some applications because of the indirect estimation from backscattering coefficient • Challenging geometry because of the obliquely oriented antenna • Incidence angle dependencies • Similarity of wind roughened water and ice on the ocean surface

ship velocity estimation [195], refugee monitoring [196], chlorophyll content [197], oil and gas reserves [198], salinity [199], microplastic pollution detection [200], turbidity and ocean color [197], and submarine detection [201], [202].

V. ADVANTAGES AND DISADVANTAGES

A. General Point of View

SAR systems are capable of acquiring very rich EO data with different characteristics, regardless of the weather and sunlight conditions. These capabilities make SAR systems an ideal tool for ocean studies. However, interpreting SAR images is usually not straightforward. For instance, speckle noise in the SAR images, as well as various effects, such as foreshortening or shadowing, make the processing and interpretation of SAR images relatively challenging. Table II summarizes the main advantages and disadvantages of SAR systems for ocean studies. More details are also provided in the following.

1) SAR systems are almost independent of the weather condition, cloud cover, and solar illumination [203]. Contrary to optical sensors that rely on the solar illumination for imaging, SAR sensors are active and transmit EM waves and receive the backscattered energy. Furthermore, the longer wavelength of the SAR systems enables them to pass through the thick clouds and acquire data in cloudy conditions [203].
2) Recent advances in SAR systems have provided very high-resolution SAR images with different data acquisition modes. Some of the advanced SAR systems can provide meter-level spatial resolutions [204], [205] and many different imaging modes that each can be used for a specific oceanographic application [205].
3) SAR images over oceans can be acquired in low-, moderate, and high-wind speed conditions, and as discussed in Section IV-A, different characteristics of the wind can be retrieved from SAR images [206].
4) With different imaging modes, SAR systems provide wide spatial coverage, which is an advantage for large-scale ocean studies [207], [208], [209].
5) SAR images can be acquired in different frequencies and polarizations. There are many different characteristics associated with each of these frequencies and polarizations that make them more suitable and informative for a specific application [210], [211].
6) Due to the higher wavelength of the microwave signals, SAR can penetrate into shallow water, snow, ground [212], [213]. Depth of the penetration depends on both the sensor characteristics (e.g., incident angle, and imaging frequency) and physical characteristics of the target (e.g., moisture, and turbidity) [212], [213].
7) SAR images are capable of providing a wide range of information about the imaging surface or object, including physical (e.g., dielectric constant, surface roughness, etc.), chemical (e.g., moisture content, etc.), and geometrical (e.g., shape, cross section, etc.) properties [31].In addition to the above-mentioned advantages, SAR systems can efficiently be used for many near-real-time applications, they are sensitive to small roughness changes on the ocean surface, and provide image-based measurements which make them suitable for various oceanographic applications.

Despite many advantages of SAR systems for ocean applications, there are also several challenges which are briefly discussed as follows.

1) The complexity of SAR images has made the interpretation of SAR images very challenging. As a result, advanced machine learning and data mining algorithms are sometimes required for SAR data processing [214], [215], [216].
2) SAR data requires advanced pre-processing steps for SAR image formation (i.e., SAR data focusing) [217] and SAR image enhancement [218], [219], before being used in advanced data processing algorithms.
3) Due to the coherent imaging mechanism, SAR images suffer from multiplicative speckle noise effect. Speckle in SAR images makes image processing and understanding more challenging. Thus, speckle reduction filters are necessary for many applications [206], [220].
4) Some geometric features of SAR systems cause geometric distortions (including foreshortening, layover, and

shadow) that can be problematic for different applications [145], [221].

5) SAR is a side-looking system and oblique SAR imaging creates complicated geometric and radiometric properties for SAR data [222]. Oblique SAR images are most problematic for image fusion with nonoblique optical images [222].
6) Due to the side-looking geometry, SAR backscattered signals considerably depend on the incidence angle of the system. The incidence angle dependency affects the classification results, especially sea ice detection and classification. The normalization techniques have been suggested in some literature to reduce this effect [223], [224], [225].
7) SAR images contain both amplitude and phase information and naturally are in complex domain. However, most of the developed data processing and machine learning algorithms are designed for real-valued data, and are not compatible with complex-valued SAR images. Thus, the phase component of SAR images has been neglected in many applications, which resulted in losing a lot of informative data. In recent years, a few studies suggested complex-valued methods which exploited both the amplitude and phase information of SAR images. However, much more studies in this field are necessary [226], [227], [228], [229], [230].
8) Relatively long revisit time of spaceborne SAR satellites limit the continues monitoring of some oceanographic phenomena, such as oil spills [31]. In addition to the abovementioned limitations of SAR systems, other factors, such as the indirect measurement of various phenomena from SAR images in oceans, make SAR data processing more challenging.

A. *Application-Based Point of View*

Table III summarizes the application-based advantages and disadvantages of SAR systems for the ocean. More details of these advantages and limitations are provided below.

For instance, the strong modulation of the Doppler with respect to the wind direction and the relationship between the wind waves and the Doppler from SAR data enables the surface wind vector retrieval from SAR data [231]. Although scatterometers are proved to be very powerful tools for wind measurements, the ability of SAR imagery systems to acquire cross-polarized data has attracted many interests. Generally, the cross-polarization signal has a high sensitivity to the wind effects on the ocean surface and has inspired to add the cross-polarized channel to the next generation scatterometers, such as Metop-Second Generation mission [231], [232]. Moreover, SAR systems provide wind data with higher spatial resolutions compared to scatterometers. However, unlike the scatterometers, SAR systems only have one antenna (i.e., one measurement), which restricts the inverse problem in scatterometry approaches for wind retrieval [231].

Considering the ocean surface current measurements, the wave mode imagery in SAR systems is beneficial for routine tracking of ocean swell fields [231]. However, the wave mode SAR images get blurred due to the wave orbital velocities, which limit the wave spectrum measurements of the short wind waves [231]. The other advantage of SAR systems for ocean surface current measurements is that SAR is the only satellite system that can measure the wave heights in ice-covered areas [231].

Although SAR is not the primary system for sea height measurement, geodetic SAR offers a relatively cost-efficient and simple technique to connect the ocean tide gauges to the global geometric network. However, several considerations should be taken into account while installing the SAR transponders. These include installing as close as possible to the tide gauges and the permanent GNSS station, avoiding the bright background or spurious signals from nearby structures like buildings or the obstacles above 20° elevation shall [233]. In addition, the number of the observations by active transponders, that are usually used in geodetic SAR systems, is very fewer than the current systems (e.g., GNSS observations) [123]. Therefore, geodetic SAR cannot be used for measuring temporal coordinate variations with shorter temporal resolution than a month [233]. Furthermore, consistent spatiotemporal modelling and correction of the SAR observations are necessary and should be provided in geodetic SAR systems [233].

High spatial resolution and wide coverage of SAR measurements are proved to be beneficial for monitoring high amplitude and hotspots of the ocean internal waves [234]. The high amplitude ocean internal waves appear as dark and bright bands in SAR images, which is relatively distinguishable [235]. However, the damping effect of the oils and films on the surface capillary waves can also manifest as bright and dark features in SAR images. This increases the uncertainty of ocean internal waves detection in SAR images [235]. Moreover, strong near-surface winds can decrease the ability of SAR to detect the sea surface signatures of the internal waves [234]. Moreover, most of the proposed approaches for internal wave detection on SAR images require human expert supervision and involve a lot of manual work. Automation is necessary for the practical applications of these approaches [235]. In this regard, numerical modelling can be utilized for automation. The required input parameters, such as the frequency, amplitude, depth, latitude and longitude, can also be extracted from the SAR images [98].

Several characteristics of sea ice, including ice coverage, thickness, ice charts, ice surface roughness, shape and orientation, snow cover, and wetness, can directly/indirectly be derived from SAR images [106]. Although SAR systems provide a pan-Arctic view of the deformation features of the sea ice, they are limited to deformation length scales of typically more than 1 km and with a monthly timescale [231]. Moreover, although near-instantaneous (subhourly) surface displacements of the sea ice can be measured by the Doppler analysis of the SAR images, the measurement is limited to one component of the ice drift due to the sparse sampling [231], [236]. Another challenge of sea ice studies with SAR images is that the backscattering from water and some ice types can be close or lower than the noise equivalent sigma zero, which complicates the interpretation of the SAR image [237]. In addition, the backscattered signal from the water can be affected by the incidence angle, wave and wind conditions, which introduces more challenges to the sea ice studies with SAR images [237]. Moreover, imaging geometry,

TABLE III
SUMMARY AND POINT-WISE ADVANTAGES AND DISADVANTAGES OF SAR SYSTEMS FOR DIFFERENT OCEANOGRAPHIC APPLICATIONS

Application	Advantage	Disadvantage
Ocean Surface Wind	• Strong relationship between the Doppler in SAR data and wind waves for inversion schemes. • Unlike scatterometers, SAR systems include cross-polarized channel.	• Unlike scatterometers, SAR systems have only one antenna, which restricts the inverse problem in scatterometry approaches. • Sparse and heterogeneous measurements.
Ocean Surface current	• Wave mode imagery in SAR systems is well-suited for routine tracking of ocean swell fields. • Only satellite system that can measure the wave heights in ice-covered regions.	• The wave orbit velocities blur the wave mode SAR images, which limits the wave spectrum measurements of the short wind waves. • Sparse and heterogeneous measurements.
Sea level	• Geodetic SAR systems offer a relatively cost-efficient and simple technique to connect the ocean tide gauges.	• Cannot be used for measuring temporal coordinate variations with shorter temporal resolution than a month. • Several considerations should be considered, including the installation condition and practical primary requirements.
Ocean internal waves	• High spatial resolution and wide coverage of SAR are helpful for high amplitude ocean internal waves. • Appear as dark and bright features in SAR images, which is relatively distinguishable. • The required input parameters of the numerical models can be extracted from SAR images.	• The damping effect of the oils and films on the surface capillary waves can also manifest as bright and dark bands in SAR images. • Strong near-surface winds can decrease the ability of SAR to detect the internal waves. • Most of the proposed approaches require human expert supervision and manual work. • Sparse and heterogeneous measurements.
Sea ice	• Many different characteristics of sea ice, including ice coverage, thickness, ice charts, shape and orientation, snow cover, and wetness, can be derived from SAR images. • Pan-Arctic view of the deformation features of the sea ice. • Near-instantaneous (sub-hourly) surface displacements can be measured by Doppler analysis of SAR.	• Limited to the large length scale deformations and a monthly timescale. • The Doppler analysis is limited to one component of the ice drift, due to the sparse sampling. • Backscattering from water and some ice types might be close or lower than the noise equivalent sigma zero of the SAR system. • The backscattering from water varies with the incidence angle, wave and wind condition. • Very sensitive to the imaging geometry, speckle noise, blurring of edges, and strong anisotropies.
Iceberg	• Pan-Arctic view. • Polarimetric SAR data increase the ability of iceberg detection.	• Different features on SAR images, such as sea ice, rough water, and snow, can have similar backscattering signatures as icebergs. • Icebergs have a broad range of backscattering signature, due to their high variability in shape, size, and texture. • Polarimetric SAR images are not sufficiently available and the spatial coverage is limited.
Aquatic vegetation and coral reef	• Penetration capability. • Can detect structure information and physical properties of the plants. • Underwater topography information can be derived from SAR images.	• The detection accuracy is heavily influenced by the incident angle. • Speckle increases the misclassification of aquatic vegetation. • Urban area and bare soil might have similar backscattering signature in coastal areas.
Ship detection	• Ships appear as bright targets in the SAR images, and are very distinguishable from the dark surrounding water surface.	• Ships have a broad diversity in structure, scale, and shape, which makes the detection more difficult. • The speckle effect in SAR images, the water surface clutter, and the complex inshore backgrounds.

TABLE III
(CONTINUE)

		• Target defocusing and the sidelobes in the strong backscattering from the ships in SAR images. • Heavily-tailed and/or bimodal histograms of SAR images.
Oil spill	• Oil films appear as dark spots on SAR images. • Oil spill Polarimetric SAR systems can discriminate between the backscattering signature from the oil spill and its lookalikes. • Inhomogeneous backscattering behavior can be used in statistical analysis for oil spill detection.	• Similar backscattering of the oil spill and its lookalikes. • Polarimetric SAR has a narrow swath width. • Various changes occur on the mineral oil film condition and creates ambiguous backscattering behavior. • Contaminated with instrument noise as the backscattering power from oil covered areas can be near or lower than the noise level of the instrument.
Ocean tide	• SAR is sensitive to the surface roughness changes, caused by the tidal waves and appear as vertical or horizontal strips in SAR image. • The tidal waves cause phase differences in the backscattered SAR signal and can be used for tidal flat monitoring.	• Several additional phenomena, such as winds and currents, also modulate the surface roughness and appear in SAR images. • The long revisit time of the available SAR satellites. • Speckle noise in SAR images complicates the edge detection for waterline extraction in tidal flat studies.
Eddies	• The wide range and high geometric resolution of SAR systems. • The shear flow at the edge of the eddy modulates the surface roughness and can be detected in SAR images as bright or dark lines. • The peak winds of the hurricane strongly interact with the ocean surface and result in vertical wind shears and turbulent eddies that can be detected on SAR images. • Availability of large coverage of the SAR systems and the long-time archive.	• The shear flow has an insignificant effect on the surface roughness. • The surface roughness is very sensitive to the wind condition and strong wind condition disrupt the effect of the shear flow on ocean surface and complicates the eddies detection from SAR images. • Most mesoscale eddies are tens of kilometers in size, and often SAR images do not cover the entire eddy. • Automation is necessary in eddy detection algorithms using SAR images.
Bathymetry	• SAR indirectly measures the bathymetry and can provide a potential solution for turbid aquatic environments. • Suitable for fast changing bathymetry environments. • The required parameters for the linear dispersion relation for water depth estimation can be extracted from SAR images.	• Availability of several inherent uncertainties in the measurement. • Not reliable enough to be utilized in practical operations. • Favorable environmental conditions are required for feature detection under shallow waters with SAR. • Knowledge of the ocean wind and current conditions are necessary for practical operations.

speckle noise, blurring edges, and the strong anisotropy in SAR imagery make sea ice monitoring more difficult [116].

The pan-Arctic view of the SAR imagery systems is also very useful for iceberg studies [128], [231]. However, iceberg detection using SAR images is not straightforward because many other features in the SAR image, including ships, very wavy water surface, and snow-covered islands could produce similar backscattering signatures and can be misclassified as iceberg or vice versa [128]. Polarimetric SAR images are proved to increase the detection accuracy of icebergs [238], but the availability and spatial coverage of polarimetric SAR are not usually sufficient to adequately study the icebergs [128]. Moreover, icebergs have a broad range of variability in size, texture, and shape, due to the environmental conditions. This creates diverse backscattering signatures for icebergs and complicates the detection procedure on SAR images [128], [239].

The main advantage of SAR systems for above/under water vegetation studies is the penetration capability of SAR signals into the vegetation canopy and water to some extend [137]. Optical and LiDAR data are the most frequently used satellite data for aquatic vegetation studies [132], [240]; however, SAR systems are also proved to be very useful for deriving information about the plant structure and physical properties, especially over shallow waters [241]. Moreover, the ability of SAR systems to detect underwater topography, due to the sea surface roughness variations, is helpful for underwater vegetation monitoring [19]. However, the detectability of above/under water vegetation on SAR images is heavily influenced by the incident angle [137]. The undesirable speckle effect of SAR images is another limiting factor which decreases the aquatic vegetation classification accuracy in SAR images [137]. Finally, the backscattering signature of the above-water vegetation can be very similar to

the backscattering from urban and bare soil areas, which might result in misclassification in coastal areas [137].

Due to the double-bounce backscattering mechanism from ships, they appear as bright targets in the SAR images and, thus, are very distinguishable from the dark surrounding water surface [242]. However, several conditions make the ship detection task more challenging. For instance, ships have a broad diversity in structure, scale, and shape, and the lack of detailed information make the detection inefficient and less effective [243]. Furthermore, the inherent speckle effect in SAR images, as well as the water surface clutter, and the complex inshore backgrounds make the ship detection more difficult [242], [243], [244]. Target defocusing and the sidelobes in the strong backscattering from the ships in SAR images is another problem in ship detection, especially from high-resolution SAR images [244]. Moreover, in the case of state-of-the-art SAR systems with high spatial resolution, the reduced scatterers per resolution cell lead to the increase of the measurability of the backscattering responses from distinct ground features. As a result, high-resolution SAR images from complex ocean areas have heavily-tailed and/or bimodal histograms. This means that the typical distributions used in conventional ship detection methods (e.g., CFAR) will not be able to model the SAR image and effectively detect the targets [242].

SAR is a suitable system for oil spill detection. This is because oil dampens the surface capillary waves of the ocean and appear as dark areas in SAR images [245]. Oil spill lookalikes, such as biogenic surface films, have a similar effect on SAR images and appear as darker areas than the surrounding water surface on SAR images [11]. As a result of the dampened capillary waves, the backscattering signature from the oil-covered areas is different. Consequently, polarimetric SAR systems are capable of discriminating between the oil spill and oil lookalikes in many cases. However, it should be noted that the swath width on polarimetric SAR systems is narrow, which is a disadvantage for practical oil spill monitoring exercises. In addition, using the polarimetric SAR will increase the operational cost and is not always practical [11], [245]. Oil films on the ocean surface can be affected by various complex physical, chemical, and biological processes and interact with the ocean environment. Therefore, several continuous changes could occur and diverse behavior can be expected from the mineral oil films in SAR images [11]. However, the diverse oil thickness and oil condition on the ocean surface creates a more inhomogeneous backscattering mechanism than the oil lookalikes. In this regard, statistical analysis of the backscattering mechanism can be employed for differentiating between the oil spill and its lookalikes [11]. Furthermore, the backscattering power, received to the sensor from oil-covered areas is often very low (i.e., near or even lower than the noise level of the instrument). Consequently, the calculated parameters are often contaminated by the instrument noise, which restricts the operational oil spill monitoring activities with SAR systems [11].

SAR systems are valuable for tidal wave monitoring. This is because they are sensitive to the surface roughness of the ocean. Tidal waves modulate the surface roughness of the ocean and can appear as vertical or horizontal stripes on SAR images [246], [247]. In addition, the phase difference in SAR images due to the tidal wave propagation is useful for tidal monitoring [248]. However, several additional phenomena, such as winds, currents, and underwater topography, also modulate the surface roughness and appear in SAR images. These consequently complicate the discrimination between different phenomena in SAR images [248]. Furthermore, the long revisit time of the available SAR satellites restricts the operational tidal flat monitoring practices in a relatively short time [248]. Moreover, edge detection, which is an essential processing step for waterline extraction in tidal flat monitoring, is complicated in SAR images due to the speckle noise [248].

The wide range and high geometric resolution of SAR systems are very valuable for mesoscale eddy observation [249]. The shear flow at the edge of the eddy modulates the surface roughness and can be detected in SAR images as bright or dark lines [249], [250]. Due to the warm-core nature of the hurricanes, the peak winds are at the lower level and strongly interact with the ocean surface and result in vertical wind shears and turbulent eddies that can be detected on SAR images [251]. In addition, the large coverage of the SAR systems and the long-time archive of these data provide the opportunity to study the long term impacts of the eddies on the environment [251]. However, monitoring eddies with SAR systems have several limitations. For example, the shear flow has an insignificant effect on the surface roughness [249]. Moreover, the surface roughness, which is measured in SAR images and is used for eddies detection, is very sensitive to the wind condition. In fact, strong wind conditions disrupt the effect of the shear flow on the ocean surface and complicate the eddies detection from SAR images [249], [250]. Moreover, most mesoscale eddies are tens of kilometers in size, and often SAR images do not cover the whole eddy [249]. Finally, manual work is still necessary for eddy detection algorithms from SAR images. This shows the importance of developing more automated algorithms for practical projects in future [249].

Although multispectral and hyperspectral imaging systems are frequently used for depth estimation in the water areas, SAR systems provide unique information for bathymetry measurements. In contrast to the optical systems, SAR indirectly measures the bathymetry and, as a result, can provide a potential solution for turbid aquatic environments [252]. Furthermore, SAR systems measure the relative bathymetry, rather than the absolute depth and are suitable for fast-changing bathymetries [252]. Moreover, the wavelength and wave direction of the ocean surface, which can be extracted from SAR images, are useful for the linear dispersion relation for water depth estimation [179]. However, due to the inherent uncertainties, bathymetry measurements from SAR are not reliable enough to be utilized in practical operations in comparison to other RS technologies. In fact, SAR measurements can be used for feature detection under shallow waters only in favorable environmental conditions [252]. Furthermore, ancillary information, such as tidal currents and wind conditions, are necessary for practical SAR bathymetry measurements [252].

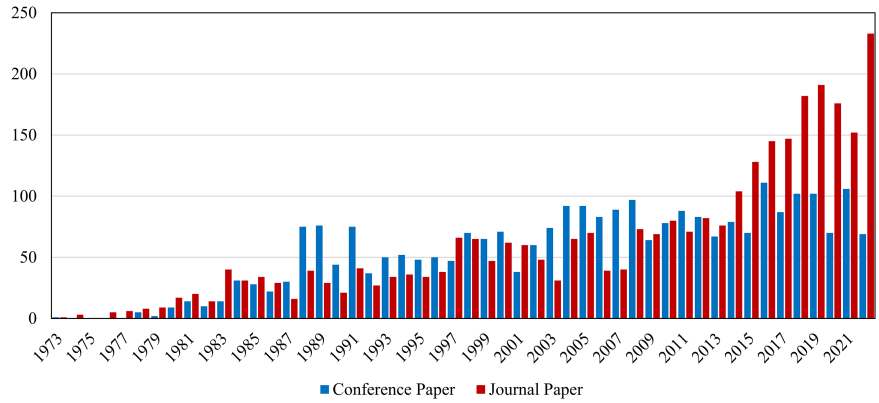

Fig. 16. Annual trend of the number of journal and conference papers published about SAR applications in the ocean.

VI. Pattern of Publication

In total, 5761 journal and conference papers (52.6% and 47.4%, respectively), published from 1973 to the end of December 2022, were investigated to present the pattern of publications about SAR applications in the ocean. In this section, the publication database preparation is explained, and then the annual publication trend, keywords analysis, and top journals and conferences are discussed. This section aims to provide concise and practical descriptions, which can be beneficial to interested readers to find the most relevant information on the SAR applications in the ocean. In addition, the extracted documents were examined to select suitable papers, providing a good overview for each ocean application using recent and highly cited papers.

A. Database Preparation

The documents for this review were gathered by a systematic literature search within the well-known database of Elsevier Scopus. In this regard, three terms of "Ocean∗" and "Synthetic Aperture Radar" or "SAR" were used to perform title/keyword/abstract query to determine English journal and conference papers from 1973 to the end of December 2022. Consistent standards for inclusion of both journal and conference documents, as well as covering a broader range of inclusion, were the reasons to use Scopus for database preparation [253]. The systematic search resulted in the selection of 5877 documents. Afterward, the journal and conference papers were subjected to a title/abstract screening to omit possible ineligible papers for further analysis. The final database contained 3034 and 2727 journal (excluding review papers) and conference papers, respectively.

B. Annual Publication Trend

The yearly publication of the relevant documents in two groups of journal and conference papers was analyzed and presented in Fig. 16. Fig. 16 shows that the number of publications (i.e., in both journal and conference categories) was lower than 80 papers per year until the end of 2003. Although the applicability of SAR data in the ocean was in its infancy, soon after, their place as a valuable data source was recognized by researchers. Later, after early studies and the availability of more SAR data, further investigations of SAR applications in the ocean attracted many other scholars. In particular, a significant rising tendency in using SAR data for oceanographic applications was started in 2014–2015, which could also be associated with the launch of Sentinel-1 by the ESA, providing open-access SAR data.

C. Keyword Analysis

A word cloud visualization generated from the keywords of the journal and conference papers is illustrated in Fig. 17. This visualization provides an overview of SAR applications in the ocean at a glance and also can present the most common applications (i.e., keywords with larger fonts). As is apparent, Synthetic Aperture Radar, RS, and Oceanography were the most frequently used keywords in the published papers, respectively. Furthermore, Sea Ice, Water Waves, Ocean Currents, Tides, and Wind were other most frequently used keywords, respectively, which also manifest the importance of these oceanographic applications using SAR data. Likewise, different satellites, including Sentinel-1, RADARSAT, Envisat-1, and TerraSAR-X, that were frequently utilized are also observable in Fig. 17.

D. Journals and Conferences

Table IV provides the top ten journals in which SAR applications in the ocean were investigated. In total, 3034 papers were published in 160 different journals. The results indicate that the leading journals were the IEEE Transactions on Geoscience and Remote Sensing, *Journal of Geophysical Research: Ocean*, *Remote Sensing*, *International Journal of Remote Sensing*, and *Remote Sensing of Environment*, each of which included more than 100 papers, publishing 35% of the relevant papers. Likewise, Table V provides five top conferences in which relevant papers were presented. In total, 2727 conference papers were presented in over 200 conferences, nearly 95% of which published less than ten papers. Based on the results, the first three conferences with the higher number of publications were the International Geoscience and Remote Sensing Symposium IGARSS, the Proceedings of SPIE The International Society for Optical Engineering, and the European Space Agency Special Publication (ESA SP Conference Proceedings).

A keywords analysis was performed for each journal to investigate the three most published oceanographic applications of SAR data in each journal (see Table VI). In this regard, the

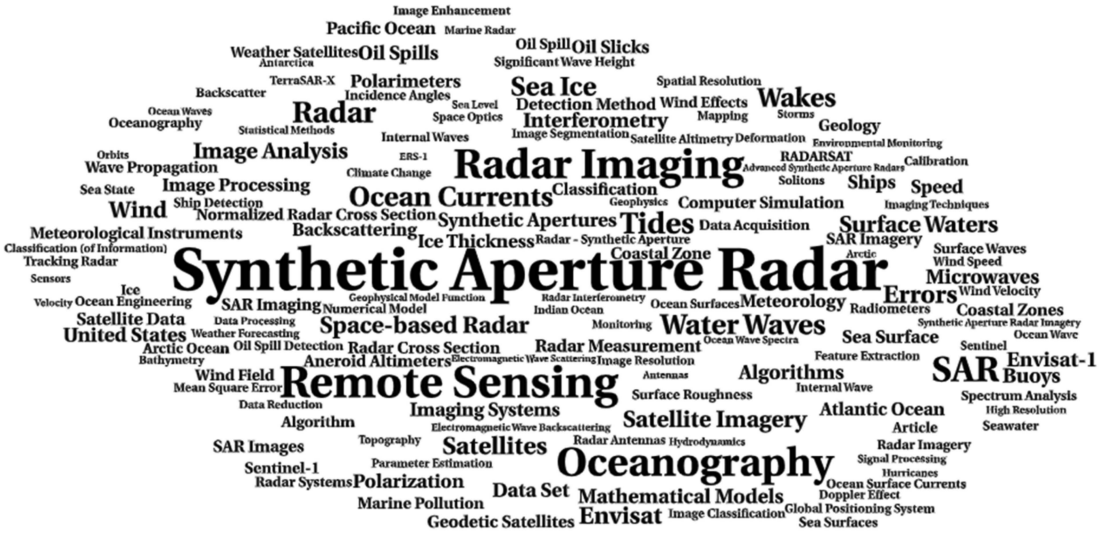

Fig. 17. Visualization of frequently used keywords in the published journal and conference papers about SAR applications in the ocean.

TABLE IV
TOP TEN JOURNALS THAT PUBLISHED OCEANOGRAPHIC APPLICATIONS OF SAR DATA

ID	Journal	# Publication
1	*IEEE Transaction on Geoscience and Remote Sensing (IEEE-TGRS)*	348
2	*Journal of Geophysical Research: Oceans* (JGR-O)*	215
3	*International Journal of Remote Sensing (IJRS)*	158
4	*Remote Sensing (RS)*	198
5	*Remote Sensing of Environment (RSE)*	114
6	*IEEE Journal of Selected Topics in Applied Earth Observations and Remote Sensing (IEEE-JSTARS)*	107
7	*Geophysical Research Letters (GRL)*	72
8	*IEEE journal of Oceanic Engineering (IEEE-OE)*	55
9	*IEEE Geoscience and Remote Sensing Letters (IEEE-GRSL)*	72
10	*Canadian Journal of Remote Sensing (CJRS)*	47

Note: Includes both *Journal of Geophysical Research* (1896–1977) and *Journal of Geophysical Research: Oceans.*

TABLE V
TOP FIVE CONFERENCES THAT PUBLISHED OCEANOGRAPHIC APPLICATIONS OF SAR DATA

ID	Conference	# Publication
1	*International Geoscience and Remote Sensing Symposium IGARSS*	1138
3	*Proceedings of SPIE The International Society for Optical Engineering*	256
2	*European Space Agency Special Publication (ESA SP Conference Proceedings)*	233
4	*Proceedings of the European Conference on Synthetic Aperture Radar EUSAR*	103
5	*Oceans Conference Record IEEE*	60

keywords of all relevant papers in each journal were considered to determine the first three applications. This may provide beneficial information for interested scholars to know relevant journals with frequent applications of SAR in the ocean.

VII. CHALLENGES AND FUTURE TRENDS

Despite the remarkable enhancements and improvements that have been made in the oceanographic studies with SAR systems, there are still several challenges that should be addressed and considered in the future. It is worth noting that some of the mentioned challenges and limitations of SAR systems for different oceanographic applications in Section V-B could also be considered valuable grounds for improving the performance of SAR systems in future studies. In this section, some of these challenges are mentioned and discussed.

Many of the oceanographic parameters, including wave, currents, and wind information, bathymetry, eddies, and tides, are indirectly derived from SAR images. As a result, many of these phenomena have direct/indirect effects on each other, and there are inherent uncertainties in SAR measurements of the ocean in comparison to other RS technologies. This in fact restricts the operational employment of SAR-based measurements in many

TABLE VI
TOP THREE OCEANOGRAPHIC APPLICATIONS OF SAR IN THE TOP TEN JOURNALS BASED ON THE KEYWORDS OF PUBLISHED PAPERS

ID	Journal	1st application	2nd application	3rd application
1	*IEEE-TGRS*	Wave	Sea Ice	Wind
2	*JGR-O*	Sea Ice	Wave	Ocean Currents
3	*IJRS*	Wave	Wind	Ocean Currents
4	*RS*	Ocean Currents	Sea Ice	Wind
5	*RSE*	Sea Ice	Ocean Currents	Wave
6	*IEEE-JSTARS*	Wind	Sea Ice	Ocean Currents
7	*GRL*	Ocean Currents	Sea Ice	Wave
8	*IEEE-OE*	Ocean Currents	Wind	Wave
9	*IEEE-GRSL*	Ship Detection	Ocean Currents	Sea Ice
10	*CJRS*	Sea Ice	Wind	Ocean Currents

Note: For the full name of each journal, see Table IV.

oceanographic activities [10], [231], [252], [254]. Therefore, it is expected that jointly deriving the oceanographic parameters will help to solve this problem to an extent and is estimated to be a future trend in this field.

Another challenge is the demand for high spatial and temporal resolution SAR images. Although many new SAR satellites have been launched in recent years and many more are planned to be launched in the future (see Section III), these SAR systems have different characteristics in terms of imaging mode, frequency, spatial resolution, polarization, and imaging geometry. State-of-the-art methods to combine the observations from different sensors in order to increase the spatial and temporal resolutions would be another development area in future studies [231], [235]. Moreover, the multisensor observations between old and new SAR satellites will enable the long-term analysis of different oceanographic phenomena and their effect on the environment [137].

Considering the massive volumes of the existing SAR data for oceanographic applications, and the data that will be acquired by the new systems, SAR oceanography can be defined as Big Data. Generally, Big Data is referred to massive and complicated datasets that are difficult to store, manage, and process with the traditional tools [255], [256]. Consequently, utilization of state-of-the-art and cloud-based Big Data processing tools, such as Google Earth Engine, for SAR oceanography is considered to be an important improvement area in this field in future studies.

Several data processing methods for deriving oceanographic parameters from SAR images include manual work, especially by domain-specific experts [98], [235], [239], [245], [257]. With the unprecedented amount of SAR data that has become available in recent years, automation for SAR data analysis is necessary. As a result, the development of completely automated SAR processing algorithms for oceanographic parameters estimation will be another trend for future studies in this field. In this regard, machine learning algorithms, and more specifically, deep learning models could significantly contribute toward developing automatic and end-to-end frameworks [150], [214], [216].

One of the advantages of new SAR systems is their wide swath width which is beneficial for various oceanographic applications. However, the effect of the incident angle on the imaging and the difference between the near and far end of the image is not negligible. Consequently, the increased swath width in SAR imagery systems and the applicability of the wide-swath images for oceanographic measurements necessitate the improvement of the incident angle invariant algorithms and necessary corrections for the mentioned differences between the near and far end of the SAR images [11], [137], [237].

Many of the targets on the ocean that can be detected in SAR images, such as ships, oil spills, sea ice, and iceberg, have broad diversity in terms of size, shape, direction, and structure, and are susceptive to fast changes in the dynamic environment of the ocean. Therefore, the development of the algorithms that are capable of detecting targets in various conditions (e.g., multiscale methods), and extraction of more conserved features would be another challenge to be tackled in future studies [11], [239], [243]. In addition, adding ancillary information to the SAR data processing chain in order to increase the reliability of the estimations, should also be considered in future studies [11], [137], [239].

VIII. CONCLUSION

The potential of SAR imagery for various oceanographic applications has been demonstrated in many studies. Many oceanographic parameters have been studied using SAR imagery since the launch of the first spaceborne SAR mission, SeaSat-1, in 1978, and even before that via airborne SAR sensors. In this review paper, a brief introduction of the interaction between the microwave waves and the ocean surface is first provided. Primary spaceborne SAR missions and the way they led to the advanced contemporary SAR sensors as well as the airborne SAR systems are then discussed. Furthermore, 12 main oceanographic applications of the SAR images, along with the advantages and disadvantages, were extensively discussed. Finally, a summary of the published articles between 1973 and the end of December 2022 about the oceanographic applications of SAR systems is presented.

Considering various studies on different applications of SAR data in the ocean, ocean wind, current, and wave are the most studied parameters due to their significance in the ocean environment. As a result of their importance for surveillance as

well as preservation concerns, ship and oil spill detection also account for a considerable portion of SAR oceanographic studies. Some of these applications have been developed sufficiently and operationally (e.g., oil spill detection). However, many other applications need to be developed and enhanced further to be applied in practical exercises, especially at global scales. In addition, the increasing number of SAR instruments and availability of high-resolution SAR images with a short revisit time have provided an unprecedented opportunity for practically employing SAR remote sensing techniques in oceanographic applications. However, the differences between the imaging characteristics of different SAR instruments should be treated conscientiously when using SAR images from various instruments. Moreover, some oceanographic applications of SAR images are not being studied anymore, as other EO images, such as optical imagery are proved to be more beneficial (e.g., direct monitoring of the fishery activities) [123]. Whereas new oceanographic applications of SAR images have been proposed in recent studies, such as Human Rights Act including refugee monitoring. More new applications are also expected to be proposed in future studies, utilizing state-of-the-art SAR systems.

Considering the crucial roles of the oceans and the increases in the destructive circumstances and incidents that threaten these sensitive environments, precise monitoring of the oceans is necessary. The superiority of SAR systems for various oceanographic applications is reviewed in this article, and is demonstrated through an increasing number of research studies being done in this field. The immense availability of SAR images with various characteristics, besides the recent advances in SAR imaging techniques, and outstanding development of various data processing and machine learning algorithms have provided a prominent opportunity for different oceanographic applications; from global-scale studies, such as global ocean currents monitoring to local-scale studies, such as coastal monitoring and ship detection. Despite the numerous studies and publications for oceanographic applications of SAR images, new technologies necessitate more advanced studies in this field. Moreover, many of these applications have not reached enough maturity to be applied in operational practices, and further studies are necessary in these fields. Therefore, more oceanographic studies using SAR images are expected in the future, especially in the field of novel applications of the new SAR imaging modes in the ocean.

REFERENCES

[1] E. National Academies of Sciences and Medicine, *A Strategy for Active Remote Sensing Amid Increased Demand for Radio Spectrum*. New York, NY, USA: Academic, 2015.

[2] R. K. Moore and W. J. Pierson, "Measuring sea state and estimating winds from a polar orbiting satellite," *InInter-. Sym. Electromagn. Sens. Earth Satell., Conv. Presentation*, Nov. 24, 1965.

[3] R. K. Moore et al., "Simultaneous active and passive microwave response of the earth-the skylab radscat experiment," *Remote Sens. Environ.*, vol. 1, pp. 189–217, 1974.

[4] P. S. Roy, M. D. Behera, and S. K. Srivastav, *Satellite Remote Sensing: Sensors, Applications and Techniques*. Berlin, Germany: Springer, 2017.

[5] C. Wang et al., "Space phased array antenna developments: A perspective on structural design," *IEEE Aerosp. Electron. Syst. Mag.*, vol. 35, no. 7, pp. 44–63, Jul. 2020.

[6] H. Guo, M. F. Goodchild, and A. Annoni, *Manual of Digital Earth*. Berlin, Germany: Springer, 2020.

[7] C. R. Jackson, J. C. B. da Silva, G. Jeans, W. Alpers, and M. J. Caruso, "Nonlinear internal waves in synthetic aperture radar imagery," *Oceanography*, vol. 26, no. 2, pp. 68–79, 2013.

[8] X. Bian, Y. Shao, C. Zhang, C. Xie, and W. Tian, "The feasibility of assessing swell-based bathymetry using SAR imagery from orbiting satellites," *ISPRS J. Photogrammetry Remote Sens.*, vol. 168, pp. 124–130, 2020.

[9] H. Fang, T. Xie, W. Perrie, L. Zhao, J. Yang, and Y. He, "Ocean wind and current retrievals based on satellite SAR measurements in conjunction with buoy and HF radar data," *Remote Sens.*, vol. 9, no. 12, 2017, Art. no. 1321.

[10] A. Wineteer et al., "Measuring winds and currents with ka-band doppler scatterometry: An airborne implementation and progress towards a spaceborne mission," *Remote Sens.*, vol. 12, no. 6, 2020, Art. no. 1021.

[11] W. Alpers, B. Holt, and K. Zeng, "Oil spill detection by imaging radars: Challenges and pitfalls," *Remote Sens. Environ.*, vol. 201, pp. 133–147, 2017.

[12] M. Amoon, A. Bozorgi, and G. Rezai-rad, "New method for ship detection in synthetic aperture radar imagery based on the human visual attention system," *J. Appl. Remote Sens.*, vol. 7, no. 1, 2013, Art. no. 71599.

[13] Y.-R. Wang and X.-M. Li, "Arctic sea ice cover data from spaceborne SAR by deep learning," *Earth Syst. Sci. Data Discuss.*, vol. 13, pp. 2723–2742, 2020.

[14] "About copernicus | CMEMS," 2021. Accessed: Sep. 13, 2021. [Online]. Available: https://marine.copernicus.eu/about

[15] D. Gao, Y. Liu, J. Meng, Y. Jia, and C. Fan, "Estimating significant wave height from SAR imagery based on an SVM regression model," *Acta Oceanologica Sinica*, vol. 37, no. 3, pp. 103–110, 2018.

[16] I. E. Kozlov, A. V. Artamonova, G. E. Manucharyan, and A. A. Kubryakov, "Eddies in the Western Arctic ocean from spaceborne SAR observations over open ocean and marginal ice zones," *J. Geophys. Res. Ocean.*, vol. 124, no. 9, pp. 6601–6616, 2019.

[17] H. Fang, W. Perrie, G. Fan, T. Xie, and J. Yang, "Ocean surface wind speed retrieval from C-band quad-polarized SAR measurements at optimal spatial resolution," *Remote Sens. Lett.*, vol. 12, no. 2, pp. 155–164, 2021.

[18] F. S. Hass and J. J. Arsanjani, "Deep learning for detecting and classifying ocean objects: Application of YoloV3 for iceberg–ship discrimination," *ISPRS Int. J. Geo-Inf.*, vol. 9, no. 12, 2020, Art. no. 758.

[19] T. Nair, L. James, C. V. Rao, A. V. V. Prasad, B. G. Krishna, and V. K. Dadhwal, "A study on the delineation of coral reefs in Andaman and Lakshadweep Islands using RISAT-1 data," *J. Indian Soc. Remote Sens.*, vol. 45, no. 5, pp. 873–885, 2017.

[20] D. P. S. Bekaert, B. D. Hamlington, B. Buzzanga, and C. E. Jones, "Spaceborne synthetic aperture radar survey of subsidence in Hampton Roads, Virginia (USA)," *Sci. Rep.*, vol. 7, no. 1, pp. 1–9, 2017.

[21] Y. Wang, M. Yang, and J. Chong, "Simulation and analysis of SAR images of oceanic shear-wave-generated eddies," *Sensors*, vol. 19, no. 7, 2019, Art. no. 1529.

[22] Y. Ren, X.-M. Li, G. Gao, and T. E. Busche, "Derivation of sea surface tidal current from spaceborne SAR constellation data," *IEEE Trans. Geosci. Remote Sens.*, vol. 55, no. 6, pp. 3236–3247, Jun. 2017.

[23] A. Johannessen et al., "Satellite oceanography from the ERS synthetic aperture radar and radar altimeter: A brief review," in *Proc. Eur. Space Agency, (Special Publication)*, 2013, pp. 201–224.

[24] Z. N. Musa, I. Popescu, and A. Mynett, "A review of applications of satellite SAR, optical, altimetry and DEM data for surface water modelling, mapping and parameter estimation," *Hydrol. Earth Syst. Sci.*, vol. 19, no. 9, pp. 3755–3769, 2015.

[25] P.-Y. Le Traon et al., "Use of satellite observations for operational oceanography: Recent achievements and future prospects," *J. Oper. Oceanogr.*, vol. 8, pp. s12–s27, 2015.

[26] J. F. Gower, "Oceans from space, a once-a-decade review of progress: Satellite oceanography in a changing world," *Oceanogr. Space*, pp. 1–12, 2010. [Online]. Available: https://doi.org/10.1007/978-90-481-8681-5_1

[27] R. Rajeesh and G. S. Dwarakish, "Satellite oceanography–A review," *Aquatic Procedia*, vol. 4, pp. 165–172, 2015.

[28] G. K. Devi, B. P. Ganasri, and G. S. Dwarakish, "Applications of remote sensing in satellite oceanography: A review," *Aquatic Procedia*, vol. 4, pp. 579–584, 2015.

[29] V. Barale, J. F. R. Gower, and L. Alberotanza, *Oceanography From Space: Revisited*. Berlin, Germany: Springer, 2010.

[30] J. L. Awange and J. B. Kyalo Kiema, "Fundamentals of Remote Sensing," *Environmental Science and Engineering*, 2013. Accessed: May 8, 2021. [Online]. Available: http://sar.kangwon.ac.kr/etc/fundam/chapter3/chapter3_1_e.html

[31] K. Sankaran, "Spaceborne radar remote sensing of ocean surfaces: Electromagnetic modelling and applications," *J. Electromagn. Waves Appl.*, vol. 34, no. 1, pp. 1–34, 2020.

[32] C. R. Jackson and J. R. Apel, Synthetic Aperture Radar: marine User's Manual, US Dept. Commerce, Washington, DC, USA, 2004.

[33] J. A. Richards, *Remote Sensing With Imaging Radar*, vol. 1. Berlin, Germany: Springer, 2009.

[34] B. Minchew, C. E. Jones, and B. Holt, "Polarimetric analysis of backscatter from the deepwater horizon oil spill using L-band synthetic aperture radar," *IEEE Trans. Geosci. Remote Sens.*, vol. 50, no. 10, pp. 3812–3830, Oct. 2012.

[35] Y. Zhang, Y. Li, X. S. Liang, and J. Tsou, "Comparison of oil spill classifications using fully and compact polarimetric SAR images," *MDPI - Appl. Sci.*, vol. 7, no. 2, 2017, Art. no. 193, doi: 10.3390/app7020193.

[36] Y. Zhang, Y. Li, and H. Lin, "Oil-spill pollution remote sensing by synthetic aperture radar," in *Proc. Adv. Geosci. Remote Sens.*, 2014, pp. 27–50.

[37] H. Zheng, J. Zhang, A. Khenchaf, and X.-M. Li, "Study on non-Bragg microwave backscattering from sea surface covered with and without oil film at moderate incidence angles," *Remote Sens.*, vol. 13, no. 13, 2021, Art. no. 2443.

[38] I. G. Rizaev, O. Karakuş, S. J. Hogan, and A. Achim, "Modeling and SAR imaging of the sea surface: A review of the state-of-the-art with simulations," *ISPRS J. Photogrammetry Remote Sens.*, vol. 187, pp. 120–140, May 1, 2022.

[39] J. B. Campbell and R. H. Wynne, *Introduction to Remote Sensing*. New York, NY, USA: Guilford Press, 2011.

[40] C. Elachi and J. J. Van Zyl, *Introduction to the Physics and Techniques of Remote Sensing*. Hoboken, NJ, USA: Wiley, 2021.

[41] J. Hausman et al., "The evolution of the PO. DAAC: Seasat to SWOT," *Adv. Space Res.*, vol. 68, pp. 1187–1193, 2021.

[42] P. A. Rosen, "Innovations in synthetic aperture radar for earth applications-past, present, and future," *JPL Open Repository*, 2017. [Online]. Available: https://hdl.handle.net/2014/48819

[43] G. Kroupnik, D. De Lisle, S. Côté, M. Lapointe, C. Casgrain, and R. Fortier, "RADARSAT constellation mission overview and status," in *Proc. IEEE Radar Conf.*, 2021, pp. 1–5.

[44] S. Abdalla and H. Hersbach, "The technical support for global validation of ERS wind and wave products at ECMWF," Eur. Space Agency, Paris, France, ECMWF Contract Rep., vol. 40, 2008. [Online]. Available: http://www.ecmwf.int/publications/library/ecpublications/_pdf/esa/ESA_abdalla_hersbach_20901-2008.pdf

[45] S. Zhang, Y. Xuan, J. Li, T. Geng, X. Li, and F. Xiao, "Arctic sea ice freeboard retrieval from Envisat altimetry data," *Remote Sens.*, vol. 13, no. 8, 2021, Art. no. 1414.

[46] P. Potin et al., "Copernicus Sentinel-1 constellation mission operations status," in *Proc. IEEE Int. Geosci. Remote Sens. Symp.*, 2019, pp. 5385–5388.

[47] S. Buckreuss et al., "Ten years of TerraSAR-X operations," *Remote Sens.*, vol. 10, no. 6, 2018, Art. no. 873.

[48] S. Sobue, T. Fukuda, H. Kamimura, O. Ochiai, A. Noda, and T. Miyashita, "Alos-2 operation status," in *Proc. IEEE Int. Geosci. Remote Sens. Symp.*, 2019, pp. 5267–5270.

[49] T. Zhang et al., "Deep learning based sea ice classification with gaofen-3 fully polarimetric SAR data," *Remote Sens.*, vol. 13, no. 8, 2021, Art. no. 1452.

[50] M. Dabboor et al., "Results update on the performance of the radarsat constellation mission," in *Proc. IEEE Int. Geosci. Remote Sens. Symp.*, 2022, pp. 4427–4430.

[51] Y. Okada et al., "System design of wide swath, high resolution, full polarimietoric L-band SAR onboard ALOS-2," in *Proc. IEEE Int. Geosci. Remote Sens. Symp.*, 2013, pp. 2408–2411.

[52] V. Klemas, "Airborne remote sensing of coastal features and processes: An overview," *J. Coastal Res.*, vol. 29, no. 2, pp. 239–255, 2013.

[53] C. E. Jones and B. Holt, "Experimental L-band airborne SAR for oil spill response at sea and in coastal waters," *Sensors*, vol. 18, no. 2, 2018, Art. no. 641.

[54] "AIRSAR - JPL," 2008. Accessed: Sep. 2021. [Online]. Available: https://airsar.jpl.nasa.gov/

[55] G. Gao, K. Huang, S. Gao, J. He, and X. Zhang, "Ship detection based on oceanic displaced phase center antenna technique in along-track interferometric SAR," *IEEE J. Sel. Topics Appl. Earth Observ. Remote Sens.*, vol. 12, no. 3, pp. 788–802, Mar. 2019.

[56] "UAVSAR - JPL," 2021. Accessed: Sep. 2021. [Online]. Available: https://uavsar.jpl.nasa.gov/

[57] R. Horn et al., "F-SAR-recent upgrades and campaign activities," in *Proc. 18th Int. Radar Symp.*, 2017, pp. 1–10.

[58] T. Kobayashi, S. Kojima, J. Uemoto, A. Nadai, M. Satake, and T. Matsuoka, "Observation of the eastern Japan great earthquake disaster with the X-band airborne SAR system (Pi-SAR2) of NICT," in *Proc. IEEE Int. Geosci. Remote Sens. Symp.*, 2019, pp. 4758–4761.

[59] R. L. Jordan, "The Seasat-A synthetic aperture radar system," *IEEE J. Ocean. Eng.*, vol. 5, no. 2, pp. 154–164, Apr. 1980.

[60] M. Amani et al., "Ocean remote sensing techniques and applications: A review (Part I)," *Water*, vol. 14, no. 21, 2022, Art. no. 3400.

[61] M. Amani et al., "Ocean remote sensing techniques and applications: A review (Part II)," *Water*, vol. 14, no. 21, 2022, Art. no. 3401.

[62] Y. Lu, B. Zhang, W. Perrie, A. A. Mouche, X. Li, and H. Wang, "A C-band geophysical model function for determining coastal wind speed using synthetic aperture radar," *IEEE J. Sel. Topics Appl. Earth Observ. Remote Sens.*, vol. 11, no. 7, pp. 2417–2428, Jul. 2018.

[63] H. Hersbach, A. D. Stoffelen, and S. de Haan, "An improved C-band scatterometer ocean geophysical model function: CMOD5," *J. Geophys. Res. Ocean.*, vol. 112, no. C3, 2007, Art. no. C03006.

[64] H. Lin, Q. Xu, and Q. Zheng, "An overview on SAR measurements of sea surface wind," *Prog. Natural Sci.*, vol. 18, no. 8, pp. 913–919, 2008.

[65] X. Yang, X. Li, Q. Zheng, X. Gu, W. G. Pichel, and Z. Li, "Comparison of ocean-surface winds retrieved from QuikSCAT scatterometer and Radarsat-1 SAR in offshore waters of the US west coast," *IEEE Geosci. Remote Sens. Lett.*, vol. 8, no. 1, pp. 163–167, Jan. 2011.

[66] B. Zhang et al., "Ocean vector winds retrieval from C-band fully polarimetric SAR measurements," *IEEE Trans. Geosci. Remote Sens.*, vol. 50, no. 11, pp. 4252–4261, Nov. 2012.

[67] G. Liu et al., "A systematic comparison of the effect of polarization ratio models on sea surface wind retrieval from C-band synthetic aperture radar," *IEEE J. Sel. Topics Appl. Earth Observ. Remote Sens.*, vol. 6, no. 3, pp. 1100–1108, Jun. 2013.

[68] V. Corcione, G. Grieco, M. Portabella, F. Nunziata, and M. Migliaccio, "A novel azimuth cutoff implementation to retrieve sea surface wind speed from SAR imagery," *IEEE Trans. Geosci. Remote Sens.*, vol. 57, no. 6, pp. 3331–3340, Jun. 2019.

[69] X.-M. Li, T. Qin, and K. Wu, "Retrieval of sea surface wind speed from spaceborne SAR over the Arctic marginal ice zone with a neural network," *Remote Sens.*, vol. 12, no. 20, 2020, Art. no. 3291.

[70] A. Corazza, A. Khenchaf, and F. Comblet, "Assessment of wind direction estimation methods from SAR images," *Remote Sens.*, vol. 12, no. 21, 2020, Art. no. 3631.

[71] L. Wang, P. Lu, and J. Ma, "Deriving sea surface wind from synthetic aperture radar based on Fourier transform and neural network," in *Proc. 10th Int. Congr. Image Signal Process., Biomed. Eng. Informat.*, 2017, pp. 1–6.

[72] Y. Wang, G. Zheng, L. Zhou, Z. Qiu, X. Li, and Y. Zhou, "Wind direction retrieval of tropical cyclone from SAR imagery using improved local gradient method," *IOP Conf. Ser.: Earth Environ. Sci.*, vol. 569, no. 1, 2020, Art. no. 12055.

[73] L. Zhou et al., "An improved local gradient method for sea surface wind direction retrieval from SAR imagery," *Remote Sens.*, vol. 9, no. 7, 2017, Art. no. 671.

[74] F. Saïd, "On the generalized curvature ocean surface scattering model for the NRCS and doppler frequency and its application to ocean surface wind retrieval from synthetic aperture radar data," doctoral thesis, UiT Arctic Univ. Norway, Tromsø, Norway, 2015.

[75] B. Yekkehkhany, *Sea Wind Vector Estimation Using C-Band Full-Polarimetric SAR Data*. Calgary, AB, Canada: Univ. Calgary, 2022.

[76] M. Denbina and M. J. Collins, "Wind speed estimation using C-band compact polarimetric SAR for wide swath imaging modes," *ISPRS J. Photogrammetry Remote Sens.*, vol. 113, pp. 75–85, 2016.

[77] V. Nilsen, G. Engen, and H. Johnsen, "A novel approach to SAR ocean wind retrieval," *IEEE Trans. Geosci. Remote Sens.*, vol. 57, no. 9, pp. 6986–6995, Sep. 2019.

[78] Y. Gao, J. Sun, J. Zhang, and C. Guan, "Extreme wind speeds retrieval using sentinel-1 IW mode SAR data," *Remote Sens.*, vol. 13, no. 10, 2021, Art. no. 1867.

[79] A. Moiseev, H. Johnsen, and J. A. Johannessen, "Retrieving ocean surface currents from the sentinel-1 doppler shift observations: A case study of the norwegian coastal current," in *Proc. IEEE Int. Geosci. Remote Sens. Symp.*, 2020, pp. 5670–5673.

[80] A. Elyouncha, "Retrieval of ocean surface currents and winds using satellite SAR backscatter and doppler frequency shift," *Remote Sens. Envorion.*, vol. 260, 2021, Art. no. 112455.

[81] A. Moiseev, H. Johnsen, J. A. Johannessen, F. Collard, and G. Guitton, "On removal of sea state contribution to sentinel-1 doppler shift for retrieving reliable ocean surface current," *J. Geophys. Res. Ocean.*, vol. 125, no. 9, 2020, Art. no. e2020JC016288.

[82] B. Chapron, F. Collard, and F. Ardhuin, "Direct measurements of ocean surface velocity from space: Interpretation and validation," *J. Geophys. Res. Ocean.*, vol. 110, no. C7, 2005.

[83] M.-K. Kang, H. Lee, C.-S. Yang, and W.-J. Yoon, "Estimation of ocean current velocity in coastal area using radarsat-1 SAR images and HF-radar data," in *Proc. IEEE Int. Geosci. Remote Sens. Symp.*, 2008, pp. I–413–I–416.

[84] M. A. Iqbal, A. Anghel, and M. Datcu, "Doppler centroid estimation for ocean surface current retrieval from Sentinel-1 SAR data," in *Proc. 18th Eur. Radar Conf.*, 2022, pp. 429–432.

[85] M. A. Iqbal, A. Anghel, and M. Datcu, "On the de-ramping of SLC-IW Tops SAR data and ocean circulation parameters estimation," in *Proc. IEEE Int. Geosci. Remote Sens. Symp.*, 2022, pp. 6817–6820.

[86] V. Zamparelli, F. De Santi, A. Cucco, S. Zecchetto, G. De Carolis, and G. Fornaro, "Surface currents derived from SAR doppler processing: An analysis over the Naples coastal region in South Italy," *J. Mar. Sci. Eng.*, vol. 8, no. 3, 2020, Art. no. 203.

[87] W. A. Qazi, W. J. Emery, and B. Fox-Kemper, "Computing ocean surface currents over the coastal California current system using 30-min-lag sequential SAR images," *IEEE Trans. Geosci. Remote Sens.*, vol. 52, no. 12, pp. 7559–7580, Dec. 2014.

[88] Y. Li, J. Chong, K. Sun, X. Yang, and Y. Zhao, "Accuracy and error analysis of vector measurement of ocean surface current by multi-aperture along-track interferometric SAR," *IEEE Access*, vol. 8, pp. 207551–207562, 2020.

[89] M. Sletten, S. Menk, and J. Toporkov, "Ocean surface current measurement with an interferometric UHF SAR," in *Proc. IEEE Int. Geosci. Remote Sens. Symp.*, 2019, pp. 98–101.

[90] S. Dangendorf et al., "Persistent acceleration in global sea-level rise since the 1960s," *Nature Climate Change*, vol. 9, no. 9, pp. 705–710, 2019.

[91] N. H. Idris, S. Vignudelli, and X. Deng, "Assessment of retracked sea levels from Sentinel-3A synthetic aperture radar (SAR) mode altimetry over the marginal seas at Southeast Asia," *Int. J. Remote Sens.*, vol. 42, no. 4, pp. 1535–1555, 2021.

[92] C. Poitevin, G. Wöppelmann, D. Raucoules, G. L. Cozannet, M. Marcos, and L. Testut, "Vertical land motion and relative sea level changes along the coastline of Brest (France) from combined space-borne geodetic methods," *Remote Sens. Environ.*, vol. 222, pp. 275–285, 2019.

[93] T. Gruber et al., "Geodetic SAR for height system unification and sea level research—Observation concept and preliminary results in the Baltic sea," *Remote Sens.*, vol. 12, no. 22, 2020, Art. no. 3747.

[94] D. Raucoules, G. L. Cozannet, M. de Michele, and S. Capo, "Observing water-level variations from space-borne high-resolution synthetic aperture radar (SAR) image correlation," *Geocarto Int.*, vol. 33, no. 9, pp. 977–987, 2018.

[95] V. Klemas, "Remote sensing of ocean internal waves: An overview," *J. Coastal Res.*, vol. 28, no. 3, pp. 540–546, 2012.

[96] S. Bao, J. Meng, L. Sun, and Y. Liu, "Detection of ocean internal waves based on faster R-CNN in SAR images," *J. Oceanol. Limnol.*, vol. 38, no. 1, pp. 55–63, 2020.

[97] W. Alpers, "Ocean internal waves," in *Encyclopedia of Remote Sensing*. Berlin, Germany: Springer, 2014.

[98] S. Vasavi, C. Divya, and A. S. Sarma, "Detection of solitary ocean internal waves from SAR images by using U-net and KDV solver technique," *Glob. Transitions Proc.*, vol. 2, pp. 145–151, 2021.

[99] H. Liu, W. Yang, H. Wei, C. Jiang, C. Liu, and L. Zhao, "On characteristics and mixing effects of internal solitary waves in the northern Yellow Sea as revealed by satellite and in situ observations," *Remote Sens.*, vol. 14, no. 15, 2022, Art. no. 3660.

[100] B. C. Wang Chen et al., "Classification of the global Sentinel-1 SAR vignettes for ocean surface process studies," *Remote Sens. Environ.*, vol. 234, 2019, Art. no. 111457.

[101] Y. Wan, X. Zhang, Y. Dai, L. Li, and X. Qu, "Azimuth cutoff compensation method for SAR wave observation based on multiview wave spectrum data fusion," *IEEE Access*, vol. 8, pp. 120923–120935, 2020.

[102] B. Huang and X.-M. Li, "Spaceborne SAR wave mode data as Big Data for global ocean wave observation," in *Proc. 13th Eur. Conf. Synthetic Aperture Radar*, 2021, pp. 1–6.

[103] M. J. Collins, M. Ma, and M. Dabboor, "On the effect of polarization and incidence angle on the estimation of significant wave height from SAR data," *IEEE Trans. Geosci. Remote Sens.*, vol. 57, no. 7, pp. 4529–4543, Jul. 2019.

[104] A. S. Gardner et al., "Increased west Antarctic and unchanged east Antarctic ice discharge over the last 7 years," *Cryosphere*, vol. 12, no. 2, pp. 521–547, 2018.

[105] N. Zakhvatkina, V. Smirnov, and I. Bychkova, "Satellite SAR data-based sea ice classification: An overview," *Geosciences*, vol. 9, no. 4, 2019, Art. no. 152.

[106] A. M. Johansson, C. Brekke, G. Spreen, and J. A. King, "X-, C-, and L-band SAR signatures of newly formed sea ice in Arctic leads during winter and spring," *Remote Sens. Environ.*, vol. 204, pp. 162–180, 2018.

[107] M. Arkett, D. Flett, R. De Abreu, and C. Gillespie, "Sea ice type and open water discrimination for operational ice monitoring with RADARSAT-2," in *Proc. IEEE Int. Symp. Geosci. Remote Sens.*, 2006, pp. 1631–1634.

[108] R. Ressel, S. Singha, S. Lehner, A. Rösel, and G. Spreen., "Investigation into different polarimetric features for sea ice classification using X-band synthetic aperture radar," *IEEE J. Sel. Topics Appl. Earth Observ. Remote Sens.*, vol. 9, no. 7, pp. 3131–3143, Jul. 2016.

[109] M. Dabboor, B. Montpetit, and S. Howell, "Assessment of simulated compact polarimetry of the high resolution radarsat constellation mission SAR mode for multiyear and first year sea ice characterization," in *Proc. IEEE Int. Geosci. Remote Sens. Symp.*, 2018, pp. 2420–2423.

[110] J.-W. Park, A. A. Korosov, M. Babiker, J.-S. Won, M. W. Hansen, and H.-C. Kim, "Classification of sea ice types in Sentinel-1 synthetic aperture radar images," *Cryosphere*, vol. 14, no. 8, pp. 2629–2645, 2020.

[111] A. Laforge et al., "Toward improved sea ice freeboard observation with SAR altimetry using the physical retracker SAMOSA+," *Adv. Space Res.*, vol. 68, no. 2, pp. 732–745, 2021.

[112] S. Leigh, Z. Wang, and D. A. Clausi, "Automated ice–water classification using dual polarization SAR satellite imagery," *IEEE Trans. Geosci. Remote Sens.*, vol. 52, no. 9, pp. 5529–5539, Sep. 2014.

[113] X.-M. Li, Y. Sun, and Q. Zhang, "Extraction of sea ice cover by Sentinel-1 SAR based on support vector machine with unsupervised generation of training data," *IEEE Trans. Geosci. Remote Sens.*, vol. 59, no. 4, pp. 3040–3053, Apr. 2021.

[114] M. Shokr, M. Dabboor, M. Lacelle, T. Zagon, and B. Deschamps, "Observations from C-band SAR fully polarimetric parameters of mobile sea ice based on radar scattering mechanisms to support operational sea ice monitoring," *Can. J. Remote Sens.*, vol. 48, no. 2, pp. 197–213, 2022.

[115] J. Karvonen, "Baltic sea ice concentration estimation using SENTINEL-1 SAR and AMSR2 microwave radiometer data," *IEEE Trans. Geosci. Remote Sens.*, vol. 55, no. 5, pp. 2871–2883, May 2017.

[116] S. Khaleghian, H. Ullah, T. Kræmer, N. Hughes, T. Eltoft, and A. Marinoni, "Sea ice classification of SAR imagery based on convolution neural networks," *Remote Sens.*, vol. 13, no. 9, 2021, Art. no. 1734.

[117] I. Heidarpour Shahrezaei and H.-C. Kim, "Fractal analysis and texture classification of high-frequency multiplicative noise in SAR sea-ice images based on a transform-domain image decomposition method," *IEEE Access*, vol. 8, pp. 40198–40223, 2020.

[118] S. Ramjan, T. Geldsetzer, R. Scharien, and J. Yackel, "Predicting melt pond fraction on landfast snow covered first year sea ice from winter C-band SAR backscatter utilizing linear, polarimetric and texture parameters," *Remote Sens.*, vol. 10, no. 10, 2018, Art. no. 1603.

[119] M. Liu, Y. Dai, J. Zhang, X. Zhang, J. Meng, and Q. Xie, "PCA-based sea-ice image fusion of optical data by HIS transform and SAR data by wavelet transform," *Acta Oceanologica Sin.*, vol. 34, no. 3, pp. 59–67, 2015.

[120] National Snow and Ice Data Center, "All about sea ice," 2020. Accessed: Nov. 2020. [Online]. Available: https://nsidc.org/learn/parts-cryosphere/sea-ice

[121] A. K. Mazur, A. K. Wåhlin, and A. Krężel, "An object-based SAR image iceberg detection algorithm applied to the Amundsen Sea," *Remote Sens. Environ.*, vol. 189, pp. 67–83, 2017.

[122] C. Wesche and W. Dierking, "Iceberg signatures and detection in SAR images in two test regions of the Weddell Sea, Antarctica," *J. Glaciol.*, vol. 58, no. 208, pp. 325–339, 2012.

[123] M. Amani et al., "Remote sensing systems for ocean: A review (Part 1: Passive systems)," *IEEE J. Sel. Topics Appl. Earth Observ. Remote Sens.*, vol. 15, pp. 210–234, 2022.
[124] F. M. Essary, "Icebergs A-72 and A-73 calve from larsen-d ice shelf in the weddell sea," 2021. [Online]. Available: https://usicecenter.gov/PressRelease/IcebergA72_73
[125] J. Karvonen, A. Gegiuc, T. Niskanen, A. Montonen, J. Buus-Hinkler, and E. Rinne, "Iceberg detection in dual-polarized C-band SAR imagery by segmentation and nonparametric CFAR (SnP-CFAR)," *IEEE Trans. Geosci. Remote Sens.*, vol. 60, 2022, Art. no. 4300812.
[126] M. Chini, R. Hostache, L. Giustarini, and P. Matgen, "A hierarchical split-based approach for parametric thresholding of SAR images: Flood inundation as a test case," *IEEE Trans. Geosci. Remote Sens.*, vol. 55, no. 12, pp. 6975–6988, Dec. 2017.
[127] E. Rignot, J. Mouginot, M. Morlighem, H. Seroussi, and B. Scheuchl, "Widespread, rapid grounding line retreat of Pine Island, Thwaites, Smith, and Kohler glaciers, West Antarctica, from 1992 to 2011," *Geophys. Res. Lett.*, vol. 41, no. 10, pp. 3502–3509, 2014.
[128] M. M. Barbat, C. Wesche, A. V. Werhli, and M. M. Mata, "An adaptive machine learning approach to improve automatic iceberg detection from SAR images," *ISPRS J. Photogrammetry Remote Sens.*, vol. 156, pp. 247–259, 2019.
[129] H. Heiselberg, "Ship-iceberg classification in SAR and multispectral satellite images with neural networks," *Remote Sens.*, vol. 12, no. 15, 2020, Art. no. 2353.
[130] C. Bentes, A. Frost, D. Velotto, and B. Tings, "Ship-iceberg discrimination with convolutional neural networks in high resolution SAR images," in *Proc. 11th Eur. Conf. Synthetic Aperture Radar*, 2016, pp. 1–4.
[131] G. A. Chulafak, D. Kushardono, and F. Yulianto, "Utilization of multitemporal sentinel-1 satellite imagery for detecting aquatic vegetation change in Lake Rawapening, Central Java, Indonesia," *Papers Appl. Geography*, vol. 7, pp. 316–330, 2021.
[132] E. White, M. Amani, and F. Mohseni, "Coral reef mapping using remote sensing techniques and a supervised classification algorithm," *Adv. Environ. Eng. Res.*, vol. 2, no. 4, 2021, Art. no. 1.
[133] E. Salameh et al., "Monitoring beach topography and nearshore bathymetry using spaceborne remote sensing: A review," *Remote Sens.*, vol. 11, no. 19, 2019, Art. no. 2212.
[134] Y. Hu et al., "Mapping coastal salt marshes in China using time series of Sentinel-1 SAR," *ISPRS J. Photogrammetry Remote Sens.*, vol. 173, pp. 122–134, 2021.
[135] M. P. F. Costa and K. H. Telmer, "Utilizing SAR imagery and aquatic vegetation to map fresh and brackish lakes in the Brazilian Pantanal wetland," *Remote Sens. Environ.*, vol. 105, no. 3, pp. 204–213, 2006.
[136] M. P. F. Costa, O. Niemann, E. Novo, and F. Ahern, "Biophysical properties and mapping of aquatic vegetation during the hydrological cycle of the amazon floodplain using JERS-1 and radarsat," *Int. J. Remote Sens.*, vol. 23, no. 7, pp. 1401–1426, 2002.
[137] V. Tsyganskaya, S. Martinis, P. Marzahn, and R. Ludwig, "SAR-based detection of flooded vegetation–a review of characteristics and approaches," *Int. J. Remote Sens.*, vol. 39, no. 8, pp. 2255–2293, 2018.
[138] A. Grover, S. Kumar, and A. Kumar, "Ship detection using sentinel-1 SAR data," *ISPRS Ann. Photogrammetry Remote Sens. Spatial Inf. Sci.*, vol. 4, no. 5, pp. 317–324, 2018.
[139] O. Karakuş, I. Rizaev, and A. Achim, "Ship wake detection in SAR images via sparse regularization," *IEEE Trans. Geosci. Remote Sens.*, vol. 58, no. 9, pp. 1665–1677, Sep. 1, 2020.
[140] X. Hou, W. Ao, Q. Song, J. Lai, H. Wang, and F. Xu, "FUSAR-ship: Building a high-resolution SAR-AIS matchup dataset of gaofen-3 for ship detection and recognition," *Sci. China Inf. Sci.*, vol. 63, pp. 1–19, 2020.
[141] P. Iervolino et al., "Ship detection in SAR imagery: A comparison study," in *Proc. IEEE Int. Geosci. Remote Sens. Symp.*, 2017, pp. 2050–2053.
[142] X. Chen et al., "Robust visual ship tracking with an ensemble framework via multi-view learning and wavelet filter," *Sensors*, vol. 20, no. 3, 2020, Art. no. 932.
[143] R. Touzi, J. Hurley, and P. W. Vachon, "Optimization of the degree of polarization for enhanced ship detection using polarimetric RADARSAT-2," *IEEE Trans. Geosci. Remote Sens.*, vol. 53, no. 10, pp. 5403–5424, Oct. 2015.
[144] Q. Fan et al., "Ship detection using a fully convolutional network with compact polarimetric SAR images," *Remote Sens.*, vol. 11, no. 18, 2019, Art. no. 2171.
[145] Y. Wang, C. Wang, H. Zhang, Y. Dong, and S. Wei, "A SAR dataset of ship detection for deep learning under complex backgrounds," *Remote Sens.*, vol. 11, no. 7, 2019, Art. no. 765.
[146] T. Zhang and X. Zhang, "High-speed ship detection in SAR images based on a grid convolutional neural network," *Remote Sens.*, vol. 11, no. 10, 2019, Art. no. 1206.
[147] T. Zhang, X. Zhang, J. Shi, and S. Wei, "Depthwise separable convolution neural network for high-speed SAR ship detection," *Remote Sens.*, vol. 11, no. 21, 2019, Art. no. 2483.
[148] H. Guo, X. Yang, N. Wang, and X. Gao, "A CenterNet++ model for ship detection in SAR images," *Pattern Recognit.*, vol. 112, 2021, Art. no. 107787.
[149] A. Bonnington, M. Amani, and H. Ebrahimy, "Oil spill detection using satellite imagery," *Adv. Environ. Eng. Res.*, vol. 2, no. 4, 2021, Art. no. 1.
[150] S. T. Seydi, M. Hasanlou, M. Amani, and W. Huang, "Oil spill detection based on multiscale multidimensional residual CNN for optical remote sensing imagery," *IEEE J. Sel. Topics Appl. Earth Observ. Remote Sens.*, vol. 14, pp. 10941–10952, 2021.
[151] A. Buono, F. Nunziata, C. R. de Macedo, D. Velotto, and M. Migliaccio, "A sensitivity analysis of the standard deviation of the copolarized phase difference for sea oil slick observation," *IEEE Trans. Geosci. Remote Sens.*, vol. 57, no. 4, pp. 2022–2030, Apr. 2019.
[152] B. Hassani, M. R. Sahebi, and R. M. Asiyabi, "Oil spill four-Class classification using UAVSAR polarimetric data," *Ocean Sci. J.*, vol. 55, no. 3, pp. 433–443, 2020.
[153] C. E. Jones, B. Minchew, B. Holt, and S. Hensley, "Studies of the Deepwater Horizon oil spill with the UAVSAR radar," *Geophysical Monograph Ser.*, vol. 195, pp. 33–50, 2013.
[154] H. Jafarzadeh, M. Mahdianpari, S. Homayouni, F. Mohammadimanesh, and M. Dabboor, "Oil spill detection from synthetic aperture radar earth observations: A meta-analysis and comprehensive review," *GIScience Remote Sens.*, vol. 58, no. 7, pp. 1022–1051, 2021.
[155] S. Skrunes, C. Brekke, and T. Eltoft, "Characterization of marine surface slicks by Radarsat-2 multipolarization features," *IEEE Trans. Geosci. Remote Sens.*, vol. 52, no. 9, pp. 5302–5319, Sep. 2014.
[156] Y. Li, Y. Zhang, Z. Yuan, H. Guo, H. Pan, and J. Guo, "Marine oil spill detection based on the comprehensive use of polarimetric SAR data," *Sustainability*, vol. 10, no. 12, 2018, Art. no. 4408.
[157] S. Tong, X. Liu, Q. Chen, Z. Zhang, and G. Xie, "Multi-feature based ocean oil spill detection for polarimetric SAR data using random forest and the self-similarity parameter," *Remote Sens.*, vol. 11, no. 4, 2019, Art. no. 451.
[158] D. Song, Y. Ding, X. Li, B. Zhang, and M. Xu, "Ocean oil spill classification with RADARSAT-2 SAR based on an optimized wavelet neural network," *Remote Sens.*, vol. 9, no. 8, 2017, Art. no. 799.
[159] G. Suresh, C. Melsheimer, J.-H. Körber, and G. Bohrmann, "Automatic estimation of oil seep locations in synthetic aperture radar images," *IEEE Trans. Geosci. Remote Sens.*, vol. 53, no. 8, pp. 4218–4230, Aug. 2015.
[160] S. Angelliaume et al., "SAR imagery for detecting sea surface slicks: Performance assessment of polarization-dependent parameters," *IEEE Trans. Geosci. Remote Sens.*, vol. 56, no. 8, pp. 4237–4257, Aug. 2018.
[161] M. R. A. Conceição et al., "SAR oil spill detection system through random forest classifiers," *Remote Sens.*, vol. 13, no. 11, 2021, Art. no. 2044.
[162] M. Shaban et al., "A deep-learning framework for the detection of oil spills from SAR data," *Sensors*, vol. 21, no. 7, 2021, Art. no. 2351.
[163] H. Tsuruoka, M. Ohtake, and H. Sato, "Statistical test of the tidal triggering of earthquakes: Contribution of the ocean tide loading effect," *Geophys. J. Int.*, vol. 122, no. 1, pp. 183–194, 1995.
[164] H. Han and H. Lee, "Tide deflection of Campbell Glacier Tongue, Antarctica, analyzed by double-differential SAR interferometry and finite element method," *Remote Sens. Environ.*, vol. 141, pp. 201–213, 2014.
[165] C. E. Ferguson, "A rising tide does not lift all boats: Intersectional analysis reveals inequitable impacts of the seafood trade in fishing communities," *Front. Mar. Sci.*, vol. 8, 2021, Art. no. 246.
[166] Q. Li, Y. Bing-Dong, and H. Bi-Guang, "Calculation and measurement of tide height for the navigation of ship at high tide using artificial neural network," *Polish Maritime Res.*, vol. 25, pp. 99–110, 2018.
[167] L. Padman, M. R. Siegfried, and H. A. Fricker, "Ocean tide influences on the Antarctic and Greenland ice sheets," *Rev. Geophys.*, vol. 56, no. 1, pp. 142–184, 2018.
[168] W. Wang, H. Yuan, and M. Tan, "Application of bp neural network in monitoring of ocean tide level," in *Proc. Int. Conf. Comput. Intell. Commun. Netw.*, 2015, pp. 1238–1240.
[169] R. M. Ferreira, S. F. Estefen, and R. Romeiser, "Under what conditions SAR along-track interferometry is suitable for assessment of tidal energy resource," *IEEE J. Sel. Topics Appl. Earth Observ. Remote Sens.*, vol. 9, no. 11, pp. 5011–5022, Nov. 2016.

[170] E. Ferrentino, F. Nunziata, and M. Migliaccio, "Monitoring waterline variation of the Monte Cotugno lake using dual-polarimetric SAR data," in *Proc. IEEE 3rd Int. Forum Res. Technol. Soc. Ind.*, 2017, pp. 1–4.

[171] C. T. Wild, O. J. Marsh, and W. Rack, "Differential interferometric synthetic aperture radar for tide modelling in Antarctic ice-shelf grounding zones," *Cryosphere*, vol. 13, no. 12, pp. 3171–3191, 2019.

[172] S.-H. Baek and C. K. Shum, "Estimating ocean tidal constituents using SAR interferometric time series over the Sulzberger ice shelf, W. Antarctica," *J. Korean Soc. Surveying*, vol. 36, no. 5, pp. 343–353, 2018.

[173] J. Ning, Q. Xu, H. Zhang, T. Wang, and K. Fan, "Impact of cyclonic ocean eddies on upper ocean thermodynamic response to typhoon Soudelor," *Remote Sens.*, vol. 11, no. 8, 2019, Art. no. 938.

[174] Y. Du, J. Liu, W. Song, Q. He, and D. Huang, "Ocean eddy recognition in SAR images with adaptive weighted feature fusion," *IEEE Access*, vol. 7, pp. 152023–152033, 2019.

[175] S. S. Karimova and M. Gade, "Eddies in the Red Sea as seen by satellite SAR imagery," in *Remote Sensing of the African Seas*. Berlin, Germany: Springer, 2014, pp. 357–378.

[176] A. Y. Ivanov and A. I. Ginzburg, "Oceanic eddies in synthetic aperture radar images," *J. Earth Syst. Sci.*, vol. 111, no. 3, 2002, Art. no. 281.

[177] S. Shu et al., "Performance analysis of ocean eddy detection and identification by L-Band compact polarimetric synthetic aperture radar," *Remote Sens.*, vol. 13, no. 23, 2021, Art. no. 4905.

[178] S. Karimova and M. Gade, "Improved statistics of sub-mesoscale eddies in the Baltic Sea retrieved from SAR imagery," *Int. J. Remote Sens.*, vol. 37, no. 10, pp. 2394–2414, 2016.

[179] P. Pereira, P. Baptista, T. Cunha, P. A. Silva, S. Romão, and V. Lafon, "Estimation of the nearshore bathymetry from high temporal resolution Sentinel-1A C-band SAR data-A case study," *Remote Sens. Environ.*, vol. 223, pp. 166–178, 2019.

[180] X. Bian et al., "Underwater topography detection in coastal areas using fully polarimetric SAR data," *Remote Sens.*, vol. 9, no. 6, 2017, Art. no. 560.

[181] S. Wiehle and A. Pleskachevsky, "Bathymetry derived from sentinel-1 synthetic aperture radar," in *Proc. Eur. Conf. Synthetic Aperture Radar*, 2018, pp. 747–750.

[182] G. Zhang, W. Perrie, B. Zhang, J. Yang, and Y. He, "Monitoring of tropical cyclone structures in ten years of RADARSAT-2 SAR images," *Remote Sens. Environ.*, vol. 236, 2020, Art. no. 111449.

[183] W. Ni, A. Stoffelen, and K. Ren, "Hurricane eye morphology extraction from SAR images by texture analysis," *Front. Earth Sci.*, vol. 16, pp. 190–205, 2021.

[184] G. Zhang, X. Li, W. Perrie, P. A. Hwang, B. Zhang, and X. Yang, "A hurricane wind speed retrieval model for C-band RADARSAT-2 cross-polarization ScanSAR images," *IEEE Trans. Geosci. Remote Sens.*, vol. 55, no. 8, pp. 4766–4774, Aug. 2017.

[185] S. Moretto, F. Bozzano, C. Esposito, P. Mazzanti, and A. Rocca, "Assessment of landslide pre-failure monitoring and forecasting using satellite SAR interferometry," *Geosciences*, vol. 7, no. 2, 2017, Art. no. 36.

[186] S.-W. Chen, X.-S. Wang, and S.-P. Xiao, "Urban damage level mapping based on co-polarization coherence pattern using multitemporal polarimetric SAR data," *IEEE J. Sel. Topics Appl. Earth Observ. Remote Sens.*, vol. 11, no. 8, pp. 2657–2667, Aug. 2018.

[187] M. A. Iqbal, A. Anghel, and M. Datcu, "Coastline extraction from SAR data using doppler centroid images," *IEEE Geosci. Remote Sens. Lett.*, vol. 19, 2022, Art. no. 1506205.

[188] Q. Zhu et al., "Spatiotemporal changes of coastline over the Yellow River Delta in the previous 40 years with Optical and SAR Remote Sensing," *Remote Sens.*, vol. 13, no. 10, 2021, Art. no. 1940.

[189] M. E. Shokr, Z. Wang, and T. Liu, "Sea ice drift and arch evolution in the robeson channel using the daily coverage of sentinel-1 SAR data for the 2016–2017 freezing season," *Cryosphere*, vol. 14, no. 11, pp. 3611–3627, 2020.

[190] J. M. Magalhaes, A. C. Pires, J. C. B. da Silva, M. C. Buijsman, and P. B. Oliveira, "Using SAR imagery to survey internal solitary wave interactions: A case study off the Western Iberian shelf," *Continental Shelf Res.*, vol. 220, 2021, Art. no. 104396.

[191] A. Galdelli, A. Mancini, C. Ferrà, and A. N. Tassetti, "A synergic integration of AIS data and SAR imagery to monitor fisheries and detect suspicious activities," *Sensors*, vol. 21, no. 8, 2021, Art. no. 2756.

[192] K. Takasaki, S. Uehara, M. Shimizu, and D. Inagake, "Monitoring of fishery activity using combined satellite data of SAR and nighttime visible image," in *Proc. 43rd COSPAR Sci. Assem.*, 2021, vol. 43, Art. no. 95.

[193] E. Westinga, K. Troost, L. B. Nasimiyu, P. E. Budde, and A. Vrieling, "Rapid cloud-based temporal compositing of Sentinel-1 radar imagery for epibenthic shellfish inventory," *Estuarine, Coastal Shelf Sci.*, vol. 250, 2021, Art. no. 107115.

[194] D. Sang, *A Study on Coastal Marine Atmospheric Boundary Layer Rolls Over the Gulf of Alaska Based On Sentinel-1 SAR Images*. Coral Gables, FL, USA: Univ. Miami, 2021.

[195] J. Li, L. Wang, M. Zhang, Y.-C. Jiao, and G. Liu, "Ship velocity automatic estimation method via two-dimensional spectrum pattern of Kelvin wakes in SAR images," *IEEE J. Sel. Topics Appl. Earth Observ. Remote Sens.*, vol. 14, pp. 4779–4786, 2021.

[196] P. Lanz, A. Marino, T. Brinkhoff, F. Köster, and M. Möller, "The InflateSAR campaign: Testing SAR vessel detection systems for refugee rubber inflatables," *Remote Sens.*, vol. 13, no. 8, 2021, Art. no. 1487.

[197] Y. Zhang, M. Hallikainen, H. Zhang, H. Duan, Y. Li, and X. S. Liang, "Chlorophyll-a estimation in turbid waters using combined SAR Data with hyperspectral reflectance data: A case study in Lake Taihu, China," *IEEE J. Sel. Topics Appl. Earth Observ. Remote Sens.*, vol. 11, no. 4, pp. 1325–1336, Apr. 2018.

[198] F. Nunziata, C. R. de Macedo, A. Buono, D. Velotto, and M. Migliaccio, "On the analysis of a time series of X–band TerraSAR–X SAR imagery over oil seepages," *Int. J. Remote Sens.*, vol. 40, no. 9, pp. 3623–3646, 2019.

[199] C. Li et al., "Estuarine plume: A case study by satellite SAR observations and in situ measurements," *IEEE Trans. Geosci. Remote Sens.*, vol. 55, no. 4, pp. 2276–2287, Apr. 2017.

[200] N. Davaasuren, A. Marino, C. Boardman, N. Ackermann, M. Alparone, and F. Nunziata, "Exploring the use of SAR remote sensing to detect microplastics pollution in the oceans," in *Proc. 5th Adv. SAR Oceanogr. Workshop*, A. Marino, N. Davaasuren, and C. Boardman, Eds., Frascati, Italy, May 7-11, 2018.

[201] J. Ren and J. Wang, "Simulation of SAR images of submarine wakes," in *Proc. IEEE Int. Geosci. Remote Sens. Symp.*, 2016, pp. 906–909.

[202] F. Xue, W. Jin, S. Qiu, and J. Yang, "Airborne optical polarization imaging for observation of submarine Kelvin wakes on the sea surface: Imaging chain and simulation," *ISPRS J. Photogrammetry Remote Sens.*, vol. 178, pp. 136–154, 2021.

[203] H. M. Keshk and X.-C. Yin, "Change detection in SAR images based on deep learning," *Int. J. Aeronautical Space Sci.*, vol. 21, no. 2, pp. 549–559, 2020.

[204] G. Farquharson, D. Castelletti, C. Stringham, and D. Eddy, "An update on the capella space radar constellation," in *Proc. 13th Eur. Conf. Synthetic Aperture Radar*, 2021, pp. 1–4.

[205] F. Zhang, X. Yao, H. Tang, Q. Yin, Y. Hu, and B. Lei, "Multiple mode SAR raw data simulation and parallel acceleration for Gaofen-3 mission," *IEEE J. Sel. Topics Appl. Earth Observ. Remote Sens.*, vol. 11, no. 6, pp. 2115–2126, Jun. 2018.

[206] M. Migliaccio, L. Huang, and A. Buono, "SAR speckle dependence on ocean surface wind field," *IEEE Trans. Geosci. Remote Sens.*, vol. 57, no. 8, pp. 5447–5455, Aug. 2019.

[207] M. Roccheggiani, D. Piacentini, E. Tirincanti, D. Perissin, and M. Menichetti, "Detection and monitoring of tunneling induced ground movements using Sentinel-1 SAR interferometry," *Remote Sens.*, vol. 11, no. 6, 2019, Art. no. 639.

[208] D.-B. Hong and C.-S. Yang, "Automatic discrimination approach of sea ice in the Arctic Ocean using Sentinel-1 Extra Wide Swath dual-polarized SAR data," *Int. J. Remote Sens.*, vol. 39, no. 13, pp. 4469–4483, 2018.

[209] X. Liu, Y. Wang, and S. Yan, "Interferometric SAR time series analysis for ground subsidence of the abandoned mining area in North Peixian using Sentinel-1A TOPS data," *J. Indian Soc. Remote Sens.*, vol. 46, no. 3, pp. 451–461, 2018.

[210] F. Mohammadimanesh, B. Salehi, M. Mahdianpari, B. Brisco, and M. Motagh, "Multi-temporal, multi-frequency, and multi-polarization coherence and SAR backscatter analysis of wetlands," *ISPRS J. Photogrammetry Remote Sens.*, vol. 142, pp. 78–93, 2018.

[211] S. Maleki, N. Baghdadi, A. Soffianian, M. El Hajj, and V. Rahdari, "Analysis of multi-frequency and multi-polarization SAR data for wetland mapping in Hamoun-e-Hirmand wetland," *Int. J. Remote Sens.*, vol. 41, no. 6, pp. 2277–2302, 2020.

[212] L. Huang, G. Fischer, and I. Hajnsek, "Antarctic snow-covered sea ice topography derivation from TanDEM-X using polarimetric SAR interferometry," *Cryosphere Discuss.*, pp. 1–28, 2021.

[213] J. Li and S. Wang, "Using SAR-derived vegetation descriptors in a water cloud model to improve soil moisture retrieval," *Remote Sens.*, vol. 10, no. 9, 2018, Art. no. 1370.

[214] R. Mohammadi Asiyabi, M. Datcu, A. Anghel, and H. Nies, "Complex-valued end-to-end deep network with coherency preservation for complex-valued SAR data reconstruction and classification," *IEEE Trans. Geosci. Remote Sens.*, vol. 61, 2023, Art. no. 5206417.

[215] R. M. Asiyabi and M. Datcu, "Earth observation semantic data mining: Latent dirichlet allocation-based approach," *IEEE J. Sel. Topics Appl. Earth Observ. Remote Sens.*, vol. 15, pp. 2607–2620, 2022.

[216] R. Mohammadi Asiyabi, M. Datcu, A. Anghel, and H. Nies, "Complex-valued autoencoders with coherence preservation for SAR," in *Proc. 14th Eur. Conf. Synthetic Aperture Radar*, 2022, pp. 1–6.

[217] J. Chen, G.-C. Sun, M. Xing, B. Liang, and Y. Gao, "Focusing improvement of curved trajectory spaceborne SAR based on optimal LRWC preprocessing and 2-D singular value decomposition," *IEEE Trans. Geosci. Remote Sens.*, vol. 57, no. 7, pp. 4246–4258, Jul. 2019.

[218] F. Filipponi, "Sentinel-1 GRD preprocessing workflow," *Multidisciplinary Digit. Publishing Inst. Proc.*, vol. 18, no. 1, 2019, Art. no. 11.

[219] Q. Ma, "Improving SAR target recognition performance using multiple preprocessing techniques," *Comput. Intell. Neurosci.*, vol. 2021, 2021, Art. no. 6572362.

[220] S. Liu et al., "SAR speckle removal using hybrid frequency modulations," *IEEE Trans. Geosci. Remote Sens.*, vol. 59, no. 5, pp. 3956–3966, May 2021.

[221] X. Chen, Q. Sun, and J. Hu, "Generation of complete SAR geometric distortion maps based on DEM and neighbor gradient algorithm," *Appl. Sci.*, vol. 8, no. 11, 2018, Art. no. 2206.

[222] G. Yao, X. Man, L. Zhang, K. Deng, H. Zhuang, and G. Zheng, "Registrating oblique SAR images based on complementary integrated filtering and multilevel matching," *IEEE J. Sel. Topics Appl. Earth Observ. Remote Sens.*, vol. 12, no. 9, pp. 3445–3457, Sep. 2019.

[223] M. Mäkynen and J. Karvonen, "Incidence angle dependence of first-year sea ice backscattering coefficient in Sentinel-1 SAR imagery over the Kara Sea," *IEEE Trans. Geosci. Remote Sens.*, vol. 55, no. 11, pp. 6170–6181, Nov. 2017.

[224] S. Singha, A. M. Johansson, and A. P. Doulgeris, "Robustness of SAR Sea Ice Type classification across incidence angles and seasons at L-band," *IEEE Trans. Geosci. Remote Sens.*, vol. 59, no. 12, pp. 9941–9952, Dec. 2021.

[225] M. S. Mahmud, T. Geldsetzer, S. E. L. Howell, J. J. Yackel, V. Nandan, and R. K. Scharien, "Incidence angle dependence of HH-polarized C-and L-band wintertime backscatter over Arctic sea ice," *IEEE Trans. Geosci. Remote Sens.*, vol. 56, no. 11, pp. 6686–6698, Nov. 2018.

[226] A. G. Mullissa, C. Persello, and J. Reiche, "Despeckling polarimetric SAR data using a multistream complex-valued fully convolutional network," *IEEE Geosci. Remote Sens. Lett.*, vol. 19, 2022, Art. no. 4011805.

[227] Z. Zhang, H. Wang, F. Xu, and Y.-Q. Jin, "Complex-valued convolutional neural network and its application in polarimetric SAR image classification," *IEEE Trans. Geosci. Remote Sens.*, vol. 55, no. 12, pp. 7177–7188, Dec. 2017.

[228] R. Shang, G. Wang, M. A. Okoth, and L. Jiao, "Complex-valued convolutional autoencoder and spatial pixel-squares refinement for polarimetric SAR image classification," *Remote Sens.*, vol. 11, no. 5, 2019, Art. no. 522.

[229] Z. Huang, M. Datcu, Z. Pan, and B. Lei, "Deep SAR-net: Learning objects from signals," *ISPRS J. Photogrammetry Remote Sens.*, vol. 161, pp. 179–193, 2020.

[230] J. A. Barrachina, C. Ren, C. Morisseau, G. Vieillard, and J. P. Ovarlez, "Complex-valued vs. real-valued neural networks for classification perspectives: An example on non-circular data," in *Proc. InICASSP IEEE Int. Conf. Acoust., Speech Signal Process.*, Jun. 6, 2021, pp. 2990–2994.

[231] A. B. Villas Bôas et al., "Integrated observations of global surface winds, currents, and waves: Requirements and challenges for the next decade," *Front. Mar. Sci.*, vol. 6, 2019, Art. no. 425.

[232] A. A. Mouche, B. Chapron, B. Zhang, and R. Husson, "Combined co-and cross-polarized SAR measurements under extreme wind conditions," *IEEE Trans. Geosci. Remote Sens.*, vol. 55, no. 12, pp. 6746–6755, Dec. 2017.

[233] T. Gruber et al., "Geodetic SAR for baltic height system unification and baltic sealevel research," *Remote Sens.*, vol. 14, 2021, Art. no. 3250.

[234] I. Kozlov et al., "SAR observations of internal waves in the Russian Arctic seas," in *Proc. IEEE Int. Geosci. Remote Sens. Symp.*, 2015, pp. 947–949.

[235] A. A. Kurekin, P. E. Land, and P. I. Miller, "Internal waves at the U.K. continental shelf: Automatic mapping using the ENVISAT ASAR sensor," *Remote Sens.*, vol. 12, no. 15, 2020, Art. no. 2476.

[236] T. Kræmer, H. Johnsen, C. Brekke, and G. Engen, "Comparing SAR-based short time-lag cross correlation and Doppler-derived sea ice drift velocities," *IEEE Trans. Geosci. Remote Sens.*, vol. 56, no. 4, pp. 1898–1908, Apr. 2018.

[237] W. Tan, J. Li, L. Xu, and M. A. Chapman, "Semiautomated segmentation of Sentinel-1 SAR imagery for mapping sea ice in Labrador coast," *IEEE J. Sel. Topics Appl. Earth Observ. Remote Sens.*, vol. 11, no. 5, pp. 1419–1432, May 2018.

[238] J. Bailey, A. Marino, and V. Akbari, "Comparison of target detectors to identify icebergs in quad-polarimetric SAR alos-2 images," in *Proc. IEEE Int. Geosci. Remote Sens. Symp.*, 2021, pp. 5223–5226.

[239] M. M. Barbat, T. Rackow, C. Wesche, H. H. Hellmer, and M. M. Mata, "Automated iceberg tracking with a machine learning approach applied to SAR imagery: A Weddell sea case study," *ISPRS J. Photogrammetry Remote Sens.*, vol. 172, pp. 189–206, 2021.

[240] M. Amani, C. Macdonald, S. Mahdavi, M. Gullage, and J. So, "Aquatic vegetation mapping using machine learning algorithms and bathymetric lidar data: A case study from newfoundland, Canada," *J. Ocean Technol.*, vol. 16, no. 3, 2021, Art. no. 74.

[241] M. W. Lang, S. Purkis, V. V. Klemas, and R. W. Tiner, "25 promising developments and future challenges for remote sensing of wetlands," in *Remote Sens. Wetlands - Taylor and Francis*. 2015.

[242] O. Pappas, A. Achim, and D. Bull, "Superpixel-level CFAR detectors for ship detection in SAR imagery," *IEEE Geosci. Remote Sens. Lett.*, vol. 15, no. 9, pp. 1397–1401, Sep. 2018.

[243] X. Zhang et al., "A lightweight feature optimizing network for ship detection in SAR image," *IEEE Access*, vol. 7, pp. 141662–141678, 2019.

[244] Z. Sun et al., "An anchor-free detection method for ship targets in high-resolution SAR images," *IEEE J. Sel. Topics Appl. Earth Observ. Remote Sens.*, vol. 14, pp. 7799–7816, 2021.

[245] X. Li et al., "Deep-learning-based information mining from ocean remote-sensing imagery," *Natl. Sci. Rev.*, vol. 7, no. 10, pp. 1584–1605, 2020.

[246] C. Divya, S. Vasavi, and A. S. Sarma, "Ocean internal wave detection from SAR images using particle swarm optimization," in *Proc. 3rd Int. Conf. Adv. Electron., Comput. Commun.*, 2020, pp. 1–6.

[247] S. Surampudi and S. Sasanka, "Internal wave detection and characterization with SAR data," in *Proc. IEEE Recent Adv. Geosci. Remote Sens.: Technol., Standards Appl.*, 2019, pp. 104–108.

[248] S. Zhang, Q. Xu, Z. Gang, and K. Fan, "Topographic mapping of the Subei bank tidal flats using Sentinel-1A SAR images," in *Proc. IEEE Int. Geosci. Remote Sens. Symp.*, 2018, pp. 7949–7952.

[249] J. Chen, J. Yang, R. Tao, and Z. Yu, "Mesoscale eddy detection and edge structure extraction method in SAR image," *IOP Conf. Ser., Earth Environ. Sci.*, vol. 237, no. 3, 2019, Art. no. 32010.

[250] G. Xu, J. Yang, C. Dong, D. Chen, and J. Wang, "Statistical study of submesoscale eddies identified from synthetic aperture radar images in the Luzon Strait and adjacent seas," *Int. J. Remote Sens.*, vol. 36, no. 18, pp. 4621–4631, 2015.

[251] D. Protzko, S. Guimond, and C. Jackson, "Connecting turbulent eddies in mature hurricanes through wavelet analysis on SAR and IWRAP data," in *Proc. AGU Fall Meeting Abstr.*, vol. 2020, 2020, pp. A119–0007.

[252] S. D. Jawak, S. S. Vadlamani, and A. J. Luis, "A synoptic review on deriving bathymetry information using remote sensing technologies: Models, methods and comparisons," *Adv. Remote Sens.*, vol. 4, no. 2, 2015, Art. no. 147.

[253] P. Hallinger and V.-T. Nguyen, "Mapping the landscape and structure of research on education for sustainable development: A bibliometric review," *Sustainability*, vol. 12, no. 5, 2020, Art. no. 1947.

[254] C. Danilo, "Évaluation des courants de surface océanique au moyen d'un radar à ouverture synthétique," Ph.D. thesis, Université de Bretagne occidentale, Brest, France, 2009.

[255] H. Tamiminia, B. Salehi, M. Mahdianpari, L. Quackenbush, S. Adeli, and B. Brisco, "Google Earth Engine for geo-Big Data applications: A meta-analysis and systematic review," *ISPRS J. Photogrammetry Remote Sens.*, vol. 164, pp. 152–170, 2020.

[256] M. Amani et al., "Google earth engine cloud computing platform for remote sensing Big Data applications: A comprehensive review," *IEEE J. Sel. Topics Appl. Earth Observ. Remote Sens.*, vol. 13, pp. 5326–5350, 2020.

[257] C. Chen, Y. Ma, and G. Ren, "A convolutional neural network with Fletcher–Reeves algorithm for hyperspectral image classification," *Remote Sens.*, vol. 11, no. 11, 2019, Art. no. 1325.

Reza Mohammadi Asiyabi (Member, IEEE) received the B.Sc. degree in civil engineering–geomatics–and the M.Sc. degree in geomatics engineering–remote sensing–from the K. N. Toosi University of Technology, Tehran, Iran, in 2016 and 2018, respectively, with a thesis on the enhancement of SAR data classification using Bag of Visual Words representation model. He is currently working toward the Ph.D. degree in electronics engineering, telecommunications, and information technology, with a thesis on deep learning for SAR data in the presence of adversarial samples with the University Politehnica of Bucharest (UPB), Bucharest, Romania.

He is currently an Early Stage Researcher with the EU Marie Skłodowska-Curie Innovative Training Network (ITN), MENELAOS-NT, Siegen, Germany, and a Ph.D. Researcher with the Research Center for Spatial Information (CEOSpaceTech), UPB. His current research focuses on the development of complex-valued deep architectures for SAR data applications, including compression, classification, and big data semantic mining, with a focus on physics-aware trustworthy complex-valued deep networks.

Arsalan Ghorbanian received the B.Sc. degree in geodesy and geomatics engineering, the M.Sc. degree in remote sensing, and a Ph.D. degree in remote sensing from the K. N. Toosi University of Technology, Tehran, Iran, in 2016, 2018, and 2023, respectively.

He has worked with different remote sensing datasets during his academic career, including multispectral, hyperspectral, synthetic aperture radar, and thermal infrared data. He has authored or coauthored more than 30 peer-reviewed papers in these fields. His research interests include satellite image (multispectral/SAR/hyperspectral) and video processing using statistical and machine learning methods, land cover mapping, wetlands/mangroves mapping and monitoring, vegetation trend analysis, drought monitoring, sea/ocean studies, and soil moisture estimation.

Dr. Ghorbanian has been a regular Reviewer in several international remote sensing journals and is currently a Reviewer Board member of the Remote Sensing journal. He has been a Guest Editor for two Special Issues in the Remote Sensing journal. He also serves as an Advisory Board member of the Ecological Indicators. He was recognized as an excellent student during his B.Sc. and ranked first during his M.Sc. at the K. N. Toosi University of Technology. He was also selected as the Top Researcher in 2022 during his Ph.D. at the K. N. Toosi University of Technology.

Shaahin Nazarpour Tameh was born in September 1994 in Tehran, Iran. He received the B.Sc. degree in civil and geodesy from Khaje Nasir University (KNTU), Tehran, Iran, in 2017, the M.Sc. degree in environmental engineering in 2021 from the University of Genoa, Genova, Italy, where he is currently working toward the Ph.D. degree in civil, chemical, and environmental engineering, PON program.

In addition, his study involves the utilization of hydrologic modeling and hydraulic modeling methodologies. In addition, the study of urban resilience and risk assessment is another area for research study. He has collaborated actively with researchers and others in several other disciplines of stormwater and wastewater management. He has authored or coauthored a review article and some poster and conference papers. His research is the management of urban stormwater through the use of low-impact development approaches, with an emphasis on both quantity and quality aspects.

Meisam Amani (Senior Member, IEEE) received the B.Eng. degree in geomatics engineering from the University of Tabriz, Tabriz, Iran, in 2012, the M.Eng. degree in remote sensing engineering from K.N. Toosi University of Technology, Tehran, Iran, in 2014, and the Ph.D. degree in electrical engineering from Memorial University of Newfoundland, St. John's, NL, Canada, in 2018.

He is currently a Senior Remote Sensing Engineer and the Key Specialty Leader of the Remote Sensing and Geospatial Technologies a global consulting and engineering company, called WSP, where he manages and leads various industrial, governmental, and academic remote sensing projects worldwide. Over the past 15 years, he has worked on different applications of remote sensing, including but not limited to land cover/land use classification, soil moisture estimation, drought monitoring, water quality assessment, watershed management, power/transmission line monitoring, fog detection and nowcasting, and ocean wind estimation. To do these, he has utilized various remote sensing datasets (e.g., UAV, optical, LiDAR, SAR, scatterometer, radiometer, and altimeter) along with different machine learning and Big Data processing algorithms.

Dr. Amani was an Associate Editor in IEEE JSTARS and the Guest Editor for two special issues in the Remote Sensing journal. He also serves as a regular Reviewer in about 15 international remote sensing journals. He was the recipient of the prestigious Professional Engineers and Geoscientists Newfoundland and Labrador Environmental Award in 2020 due to his contribution to wetland mapping in Canada using advanced machine learning and Big Data processing algorithms. A list of his research works, including over 100 peer-reviewed journal and conference papers, can be found at https://www.researchgate.net/profile/Meisam_Amani3.

Shuanggen Jin (Senior Member, IEEE) was born in Anhui, China, in 1974. He received the B.Sc. degree in geodesy from Wuhan University, Wuhan, China, in 1999, and the Ph.D. degree in geodesy from the University of Chinese Academy of Sciences, Beijing, China, in 2003, both in geodesy.

He is currently the Vice-President and Professor with Henan Polytechnic University, China, and also Professor at Shanghai Astronomical Observatory, CAS, Shanghai, China. His main research interests include satellite navigation, remote sensing, and space/planetary exploration. He has published more than 500 papers in peer-reviewed journals and proceedings, 20 patents/software copyrights and 12 books/monographs with more than 12 000 citations and H-index>57.

Dr. Jin has been the President of International Association of Planetary Sciences (IAPS) (2015–2019), President of the International Association of CPGPS (2016–2017), Chair of IUGG Union Commission on Planetary Sciences (UCPS) (2015–2023), the Editor-in-Chief of *International Journal of Geosciences*, Editor of *Geoscience Letters*, Associate Editor of IEEE TRANSACTIONS ON GEOSCIENCE & REMOTE SENSING and *Journal of Navigation*, Editorial Board member of *Remote Sensing*, *GPS Solutions,* and *Journal of Geodynamics*. He has received 100-Talent Program of CAS, Leading Talent of Shanghai, IAG Fellow, IUGG Fellow, Fellow of Electromagnetics Academy, World Class Professor of Ministry of Education and Cultures, Indonesia, Chief Scientist of National Key R&D Program, China, Member of Russian Academy of Natural Sciences, Member of European Academy of Sciences, Member of Turkish Academy of Sciences, and Member of Academia Europaea.

Ali Mohammadzadeh received the Ph.D. degree in remote sensing from Geomatics Engineering Faculty, K.N. Toosi University of Technology, Tehran, Iran, in 2009.

He is currently an Associate Professor and Head of LiDAR laboratory, K.N.Toosi University of Technology. He has more than 60 published journal papers. His research interests include LiDAR theory and applications, artificial intelligence, image processing and pattern recognition, physics of remote sensing, optimization, sensor calibration, disaster management in fire, dust, earthquake, and flooding. He has organized some special issues and completed several industrial and national projects. He has supervised more than 30 graduate students and is responsible for courses: "LiDAR and its applications" and "Physics of Remote Sensing."